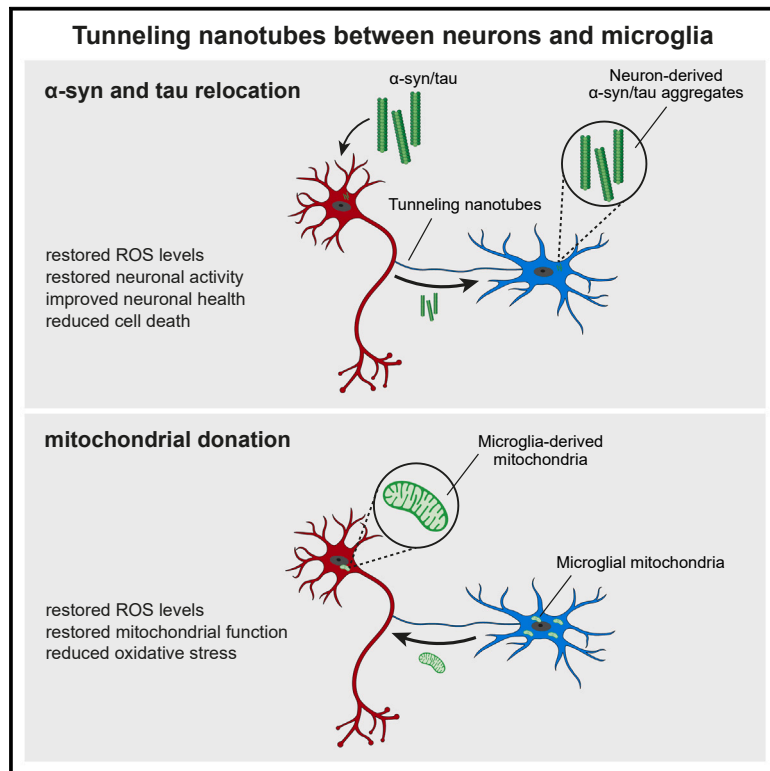


Microglia rescue neurons from aggregate-induced neuronal dysfunction and death through tunneling nanotubes

Graphical abstract



Authors

Hannah Scheiblich, Frederik Eikens, Lena Wischhof, ..., Ronald Melki, Hans-Christian Pape, Michael T. Heneka

Correspondence

michael.heneka@uni.lu

In brief

Scheiblich et al. uncover a novel mechanism by which microglia use tunneling nanotubes to connect with α -syn- or tau-burdened neurons, enabling transfer of these proteins to microglia for clearance. Microglia donate mitochondria to restore neuronal health, shedding light on new therapeutic strategies for neurodegenerative diseases.

Highlights

- α -syn and tau trigger tunneling nanotube formation between microglia and neuron
- Tunneling nanotubes facilitate the relocation of α -syn and tau into microglia
- Microglia donate healthy mitochondria to α -syn- and tau-burdened neurons
- Exchange of mitochondria rescues neurons from oxidative stress and dysfunction



Article

Microglia rescue neurons from aggregate-induced neuronal dysfunction and death through tunneling nanotubes

Hannah Scheiblich,^{1,2,3} Frederik Eikens,^{1,2,3} Lena Wischhof,^{2,3} Sabine Opitz,⁴ Kay Jüngling,⁵ Csaba Cserép,⁶ Susanne V. Schmidt,¹ Jessica Lambertz,⁷ Tracy Bellande,⁸ Balázs Pósai,⁶ Charlotte Geck,¹ Jasper Spitzer,¹ Alexandru Odainic,^{1,9} Sergio Castro-Gomez,¹⁰ Stephanie Schwartz,¹⁰ Ibrahim Boussaad,¹¹ Rejko Krüger,¹¹ Enrico Glaab,¹¹ Donato A. Di Monte,² Daniele Bano,² Ádám Dénes,⁶ Eike Latz,^{2,12} Ronald Melki,⁸ Hans-Christian Pape,⁵ and Michael T. Heneka^{2,11,12,13,14,*}

¹Institute of Clinical Chemistry and Clinical Pharmacology, University Hospital Bonn, Bonn, Germany

²German Center for Neurodegenerative Diseases, Bonn, Germany

³Max-Planck-Institute for Biology of Ageing, Cologne, Germany

⁴Institute of Neuropathology, University of Bonn, Bonn, Germany

⁵Institute of Physiology I, Westfälische Wilhelms-University Münster, Münster, Germany

⁶Institute of Experimental Medicine, Budapest, Hungary

⁷Institute of Anatomy, University Hospital Bonn, Bonn, Germany

⁸Institut François Jacob, CEA and Laboratory of Neurodegenerative Diseases, Fontenay-aux-Roses, France

⁹Department of Microbiology and Immunology, The Peter Doherty Institute for Infection & Immunity, University of Melbourne, Melbourne, VIC, Australia

¹⁰Institute of Physiology II, University Hospital Bonn, Bonn, Germany

¹¹Luxembourg Centre for Systems Biomedicine, University of Luxembourg, Belvaux, Luxembourg

¹²Institute of innate immunity, University Hospital Bonn, Bonn, Germany

¹³Department of Infectious Diseases and Immunology, University of Massachusetts, Medical School, Worcester, MA, USA

¹⁴Lead contact

*Correspondence: michael.heneka@uni.lu

<https://doi.org/10.1016/j.neuron.2024.06.029>

SUMMARY

Microglia are crucial for maintaining brain health and neuron function. Here, we report that microglia establish connections with neurons using tunneling nanotubes (TNTs) in both physiological and pathological conditions. These TNTs facilitate the rapid exchange of organelles, vesicles, and proteins. In neurodegenerative diseases like Parkinson's and Alzheimer's disease, toxic aggregates of alpha-synuclein (α -syn) and tau accumulate within neurons. Our research demonstrates that microglia use TNTs to extract neurons from these aggregates, restoring neuronal health. Additionally, microglia share their healthy mitochondria with burdened neurons, reducing oxidative stress and normalizing gene expression. Disrupting mitochondrial function with antimycin A before TNT formation eliminates this neuroprotection. Moreover, co-culturing neurons with microglia and promoting TNT formation rescues suppressed neuronal activity caused by α -syn or tau aggregates. Notably, TNT-mediated aggregate transfer is compromised in microglia carrying *Lrrk22(Gly2019Ser)* or *Trem2(T66M)* and (*R47H*) mutations, suggesting a role in the pathology of these gene variants in neurodegenerative diseases.

INTRODUCTION

The accumulation of pathological protein aggregates is a hallmark seen in several neurodegenerative diseases, including Alzheimer's disease (AD), frontotemporal dementia (FTD), and Parkinson's disease (PD). Proteins such as alpha-synuclein (α -syn) and tau, which play crucial roles in normal neuronal function, can abnormally aggregate inside cells. This aggregation disrupts

cellular processes, leading to neuronal dysfunction and contributing to the development of PD and FTD, respectively.

Pathological α -syn disrupts neuronal function through several mechanisms: it affects the proper distribution of membrane proteins,¹ interferes with neurotransmitter release,² impairs mitochondrial function,^{3–5} inhibits intracellular vesicle transport,^{6,7} disrupts endo-lysosomal compartment integrity,⁸ and compromises protein-degradation mechanisms.⁹ Conversely,



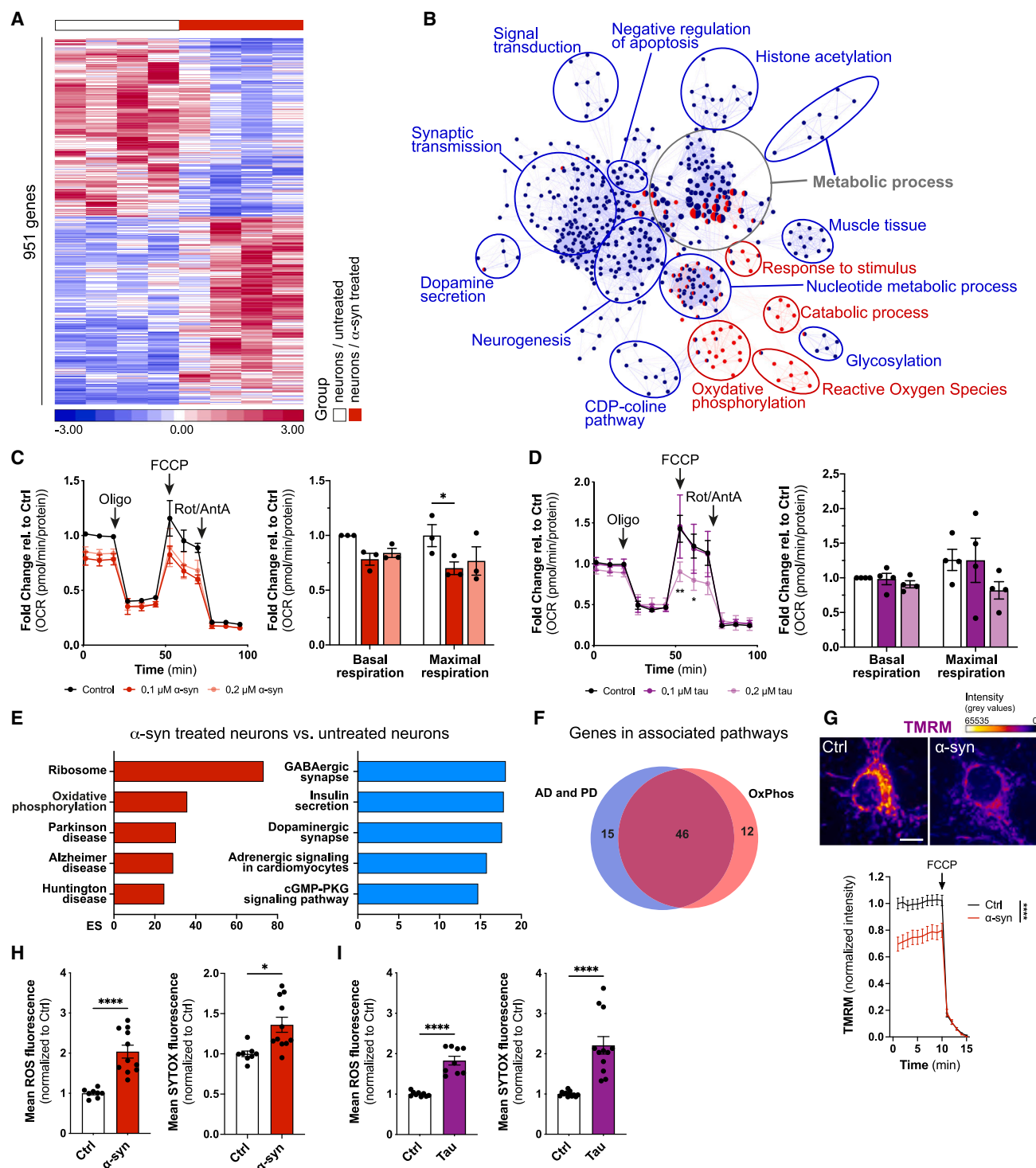


Figure 1. α -syn induces transcriptomic changes and oxidative stress in neurons

(A) Heatmap of 951 differentially expressed (DE) genes (red: induced, blue: suppressed) between control and α -syn-treated neurons.
 (B) Biological Networks Gene Ontology (BINGO) enrichment map for DE genes (red: induced, blue: suppressed) between control (Ctrl) and α -syn-treated neurons.
 (C) Oxygen consumption rate in neurons treated with fibrillar α -syn. $n = 3$, $N = 3$. * $p = 0.0314$ (Ctrl vs. 0.1 μ M).
 (D) Oxygen consumption rate in neurons treated with fibrillar tau. $n = 4$, $N = 3$. * $p = 0.0342$, ** $p = 0.0057$.
 (E) Bar charts for the top 5 enriched pathways for DE genes in α -syn-treated vs. untreated neurons. ES, enrichment score.
 (F) Overlap of genes in pathways associated with AD, PD, and OxPhos.

(legend continued on next page)

abnormally hyperphosphorylated tau contributes to neuronal dysfunction by destabilizing microtubules, compromising neuronal structure, disrupting intracellular transport,^{10,11} impairing axonal transport, and disturbing synaptic functions,¹² effectively dismantling communication between neurons.

Both α -syn and tau aggregates exhibit “prion-like” characteristics, spreading from cell to cell and inducing the misfolding of native proteins in neighboring neurons, thereby propagating neuronal damage and neurodegeneration across interconnected brain regions. Mechanisms facilitating this spread include exocytosis, endocytosis, uptake of exosome-carried proteins, direct penetration of aggregates, and formation of tunneling nanotubes (TNTs).^{13–20} Additionally, cell death induced by α -syn or tau and physiological secretion release cytotoxic proteins into the extracellular space, potentially entering cells trans-synaptically.^{21–25} These extracellular toxic proteins can initiate neuroinflammation and perpetuate neurodegenerative processes.

Microglia are integral to the brain’s innate immune system and play a crucial role in its structural remodeling and function. They maintain neuronal health and integrity through mechanisms such as synaptic scaling and pruning, as well as by releasing neurotrophic factors.²⁶ The homeostatic equilibrium of microglial cells is disrupted when pattern recognition receptors are activated by pathological protein aggregates, such as α -syn or tau, in neurodegenerative diseases.²⁷ These sterile immune stimuli may drive disease progression by releasing a multitude of immune factors, including cytokines, complement factors, and chemokines, which suppress synaptic plasticity and disrupt dendritic and axonal integrity.^{28,29} Microglia play a critical role in clearing pathological protein aggregates,³⁰ crucial for the progression of neurodegenerative diseases, as they exhibit the highest capacity among all brain cells for scavenging extracellular proteins. Yet inflammatory events can significantly impair the microglial protein clearance machinery,^{31–33} which can lead to the accumulation of protein aggregates in the brain.

Microglia are traditionally believed to encounter pathological intraneuronal protein aggregates only after their release due to neuronal cell death.^{34–37} However, our recent research has revealed that microglia form TNTs, cellular extensions that connect distant cells, including neighboring microglia, facilitating the transfer of cytotoxic protein aggregates from affected to unaffected cells and promoting protein degradation.³⁸ Additionally, we observed that naive microglia donate healthy mitochondria to rescue cells burdened with inflammation, thereby enhancing overall cell survival within the microglial population. These findings prompt the question of whether microglia play a role in preserving neuronal integrity by removing pathogenic aggregates from affected neurons via TNT formation. Recent studies have explored the exchange of cargo, including α -syn and mitochondria, between neuron- and microglia-like cell lines.³⁹ While these experiments demonstrated the transfer of α -syn and mitochon-

dria between cells, they did not elucidate the functional consequences of this exchange for cellular health. Consequently, our objective is to gain a more profound comprehension of the potential impact of this exchange on cellular functions and overall cellular health.

Here, we found that microglia establish contact with neurons through TNTs to alleviate them from cytotoxic protein accumulations. Notably, co-culturing burdened neurons with microglia revealed the transfer of intact and functional mitochondria from microglia to neurons, significantly reducing oxidative stress and enhancing neuronal health without detriment to microglia themselves. However, this protective mechanism was compromised in microglia carrying disease-modifying mutations in leucine-rich repeat kinase 2 (LRRK2) or triggering receptor expressed on myeloid cells 2 (TREM2). These findings challenge the conventional view of microglia primarily as contributors to neuroinflammation, suggesting instead a pivotal role in protecting and restoring neuronal function amidst pathological protein aggregation.

RESULTS

Microglia relieve neurons from their α -syn/tau burden

To pinpoint α -syn-induced changes in neuronal function, we performed next-generation RNA sequencing on control neurons and neurons exposed to aggregated α -syn. In total, 951 genes were differentially regulated (fold change [FC] ± 1.5 , false discovery rate [FDR] corrected p value 0.05) in response to α -syn (Figure 1A) enriched in oxidative stress-related Gene Ontology (GO) terms (Figure 1B). In line with this, oxygen consumption rate measurements showed impaired mitochondrial respiration in α -syn- or tau-loaded neurons compared to controls (Figures 1C and 1D). Partek Pathway analysis highlighted overrepresentation of genes linked to oxidative phosphorylation (OxPhos), AD, PD, and Huntington’s disease (Figure 1E). The majority of these genes were involved in OxPhos pathways (Figure 1F).

We evaluated mitochondrial membrane potential using tetramethylrhodamine methyl ester (TMRM), finding reduced levels in α -syn-treated neurons compared to controls (Figure 2G). Additionally, α -syn or tau treatment increased reactive oxygen species (ROS) and SYTOX accumulation, markers of oxidative stress and cell death (Figures 1H and 1I). These findings suggest that α -syn or tau accumulation impairs neuronal function by inducing oxidative stress and cell death.

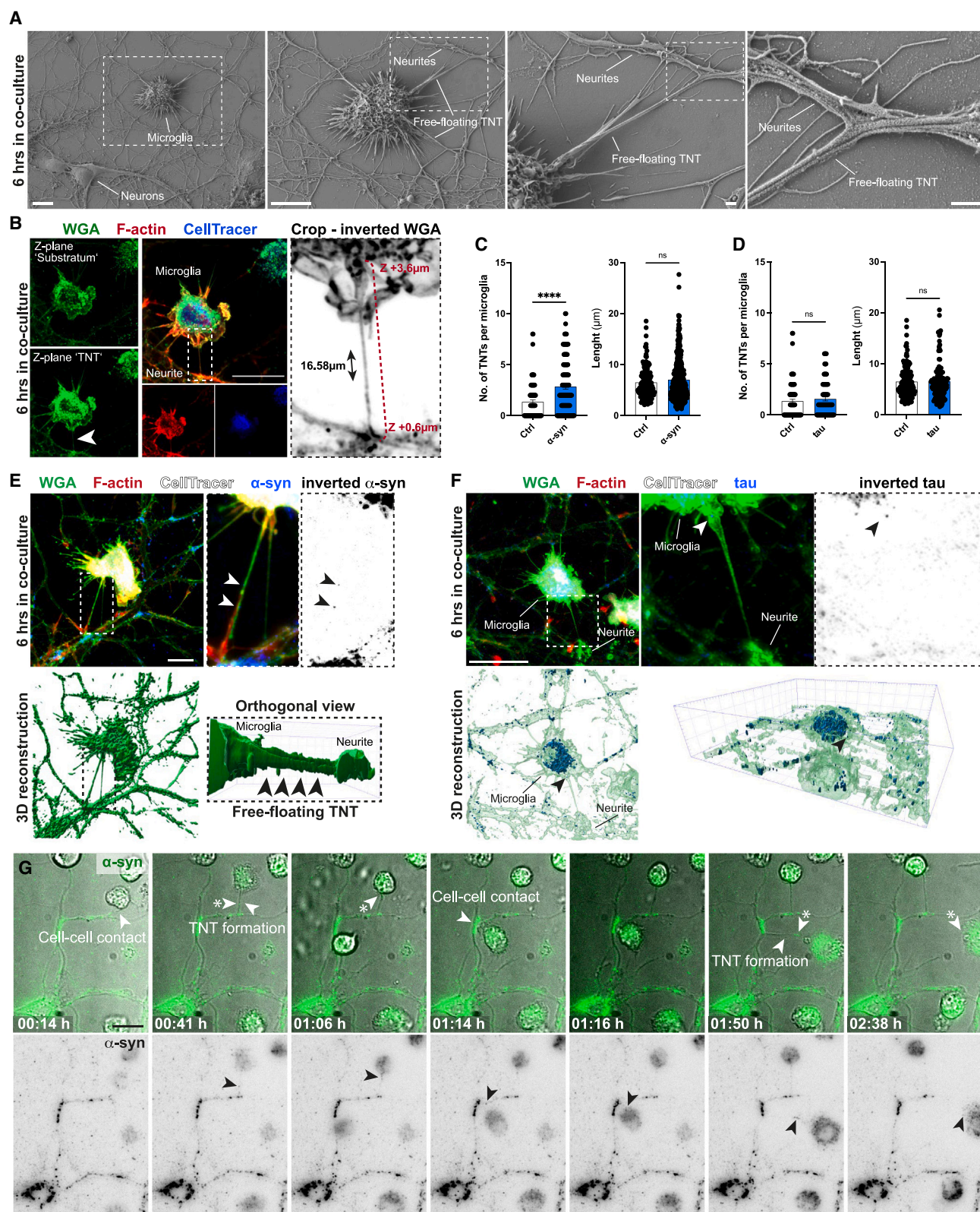
We next investigated how microglia affect α -syn-impaired neuronal health. Co-culture of primary cortical neurons and microglia led to the formation of TNTs (Figures 2A, 2B, S1A, and S1B). Unlike conventional cellular protrusions like filopodia and lamellipodia, which are anchored to the cell plate (substratum), TNTs hover freely and facilitate the exchange of cellular components between connected cells.⁴⁰ Due to the lack of a specific biomarker for TNTs, the common approach for labeling

(G) TMRM signal intensity in naive neurons and neurons treated with α -syn. $n = 3$, $N = 56$ cells. **** $p < 0.0001$. Scale bar, 10 μ m.

(H) ROS production (left) and SYTOX signal (right) in naive neurons or neurons treated with α -syn fibrils. * $p = 0.0272$ (Ctrl vs. α -syn), **** $p < 0.0001$.

(I) ROS production (left) and SYTOX signal (right) in naive neurons or neurons treated with tau fibrils. **** $p < 0.0001$.

All graphs are mean \pm SEM and were analyzed by two-way ANOVA followed by Dunnett’s test (C and D), one-way ANOVA followed by Dunnett’s test (G), or t test (H and I).



(legend on next page)

involves staining the entire plasma membrane with fluorescent proteins that bind to glycolipids and glycoproteins, like wheat germ agglutinin (WGA), or targeting their actin structure with fluorescently labeled phalloidin.⁴¹ Using their distinct free-floating morphology, we employed super-resolution three-dimensional (3D) laser scanning confocal microscopy in fixed cells to measure tube heights above the substratum based on their Z plane within the stack (Figure 2B). This method for analyzing TNTs has been previously documented.⁴⁰ Similar to previous findings in neuron-like CAD (Cath.a-differentiated) cells,¹⁹ we observed that α -syn aggregate accumulation increased the number of free-floating TNTs connecting neurons and microglia (Figure 2C), typically 5–10 μ m long, consistent with macrophage observations.⁴² We also noted TNTs between tau-loaded neurons and microglia, although their number and length did not change (Figure 2D). These TNTs contained α -syn- and tau-immunoreactive particles (Figures 2E and 2F), suggesting they facilitate the exchange of pathological proteins between neurons and microglia. This finding, along with our previous report of aggregate clearance by microglia, prompted us to investigate the functional role of TNTs in this context.³⁸

Primary cortical neurons loaded with fluorescently labeled fibrillar α -syn or tau were incubated with primary microglia for up to 6 h. We observed a time-dependent transfer of α -syn and tau from neurons to microglia through TNTs (Figures 2G, 3A–3C, and S1C–S1F and Video S1), with similar transfer features for both proteins (Figures S1G and S1H). Importantly, neurons alone could not degrade the cytotoxic protein aggregates, but adding microglia significantly reduced α -syn levels in neurons (Figure 3D). This reduction required direct contact, as transwell insert experiments showed no effect (Figures 3D and S2C). Subsequently, neuron-derived α -syn was degraded within microglia over time (Figure 3E).

Despite what is known in the literature as characteristic features of TNTs,⁴⁰ we demonstrate that TNTs can transport aggregates as non-free-floating structures between cells (Figure S1C). Notably, α -syn aggregates were transferred from neurons to microglia, but not vice versa (Figure S1I). We excluded phagocytosis of neuronal structure as the cause for aggregate presence in microglia by showing no increase in neuronal protein content over time (Figure S2A). Feeding microglia with α -syn-containing neuronal debris confirmed no degradation of neuronal debris or aggregates at any investigated time points (Figure S2B). Analyzing the neurite thickness at sites of TNT formation showed no evidence of neurite phagocytosis (Figure S2D). BSA, a non-neurotoxic protein, was also transported, indicating a general protein exchange, regardless of their toxicity (Figure S2E). Lipo-

polysaccharide (LPS) activation of microglia did not affect TNT formation or aggregate transfer (Figures S2F and S2G).

Together, our data suggest that microglia, through TNTs, can alleviate neurons from their α -syn and tau aggregates and effectively degrade the received proteins.

Intercellular transfer of α -syn depends on P2Y12R-Rac-PAK-F-actin signaling

Since TNTs are mainly composed of actin, we examined pathways upstream to understand the regulation of α -syn transfer. We identified the Rac-PAK pathways as crucial in modulating this process (Figure 3F). Inhibition of Rac or PAK significantly impeded TNT formation between neurons and microglia (Figures 3G–3K) while only slightly impairing α -syn phagocytosis in microglial cultures (Figures S3A–S3C). Rac1 knockout microglia confirmed Rac1's role in α -syn transfer (Figures S3D and S3E). Actin regulators Arp2/3 (actin-related protein 2/3) and cofilin, which modulate polymerization and depolymerization downstream of Rac, were also key regulators as inhibitors significantly affecting α -syn transfer from neurons to microglia (Figures 3L and 3M), potentially exacerbating α -syn accumulation within neurons.

P2Y12R activation facilitates actin remodeling and microglial process recruitment⁴³ upstream of Rac-PAK, with neuronal ATP/ADP release and P2Y12 signaling being essential⁴⁴ (Figure S3F). The P2Y12R antagonist PSB-0739⁴⁵ reduced TNT formation between microglia and neurons, thereby impairing α -syn aggregate transfer (Figures S3G and S3H). These findings demonstrate that microglia alleviate neuronal cytotoxic aggregates through TNTs via a P2Y12R-Rac-PAK-F-actin pathway.

Evidence for TNTs between neurons and microglia from mice and human

To further elucidate the role of neuron-microglia contacts in reducing neuronal α -syn burden, we engrafted α -syn-containing primary cortical neurons into the cortex of Cx3cr1^{GFP/+} mice and used *in vivo* two-photon laser scanning microscopy to track α -syn (Figure 4A). Microglia near the injection site formed contacts with engrafted neurons, as shown by live imaging and immunohistochemistry (Figures 4A and 4B). Most importantly, we observed α -syn aggregate transfer from neurons to microglia (Figure 4A) but could not definitively identify these connections as TNTs (Figure 4B). TNTs are characterized by their open-ended structure, directly connecting the cytoplasm of two cells without a separating plasma membrane.⁴⁶ To further gain insight into the presence of TNTs *in vivo*, we screened serial section electron microscopy of

Figure 2. Pathogenic α -syn and tau traffic within TNTs connecting neurons and microglia

(A) Electron microscopic image of free-floating TNTs between neurons and microglia. Scale bar, 10 μ m (both left), 1 μ m (both right).
(B) Immunostaining of free-floating TNTs between neurons and microglia showing Z planes over the trajectory of TNTs. Scale bar, 10 μ m.
(C) Number and length of TNTs connecting microglia to neurons treated or not with α -syn. Left: $n = 87$ (Ctrl) and 128 (α -syn) individual microglia. Right: $n = 131$ (Ctrl) and 370 (α -syn) individual TNTs. **** $p < 0.0001$.
(D) Number and length of TNTs connecting microglia to neurons treated or not with tau. Left: $n = 87$ (Ctrl) and 81 (tau) individual microglia. Right: $n = 131$ (Ctrl) and 128 (tau) individual TNTs.
(E) Immunostaining of TNTs between neurons and microglia containing α -syn aggregates. Arrowheads indicate α -syn aggregates. Scale bar, 10 μ m.
(F) Immunostaining of TNTs between neurons and microglia containing tau aggregates. Scale bar, 10 μ m.
(G) Time-lapse video of TNTs between neurons and microglia showing α -syn aggregate transfer. Scale bar, 20 μ m.
All graphs are mean \pm SEM and were analyzed by t test. See also Figure S1.

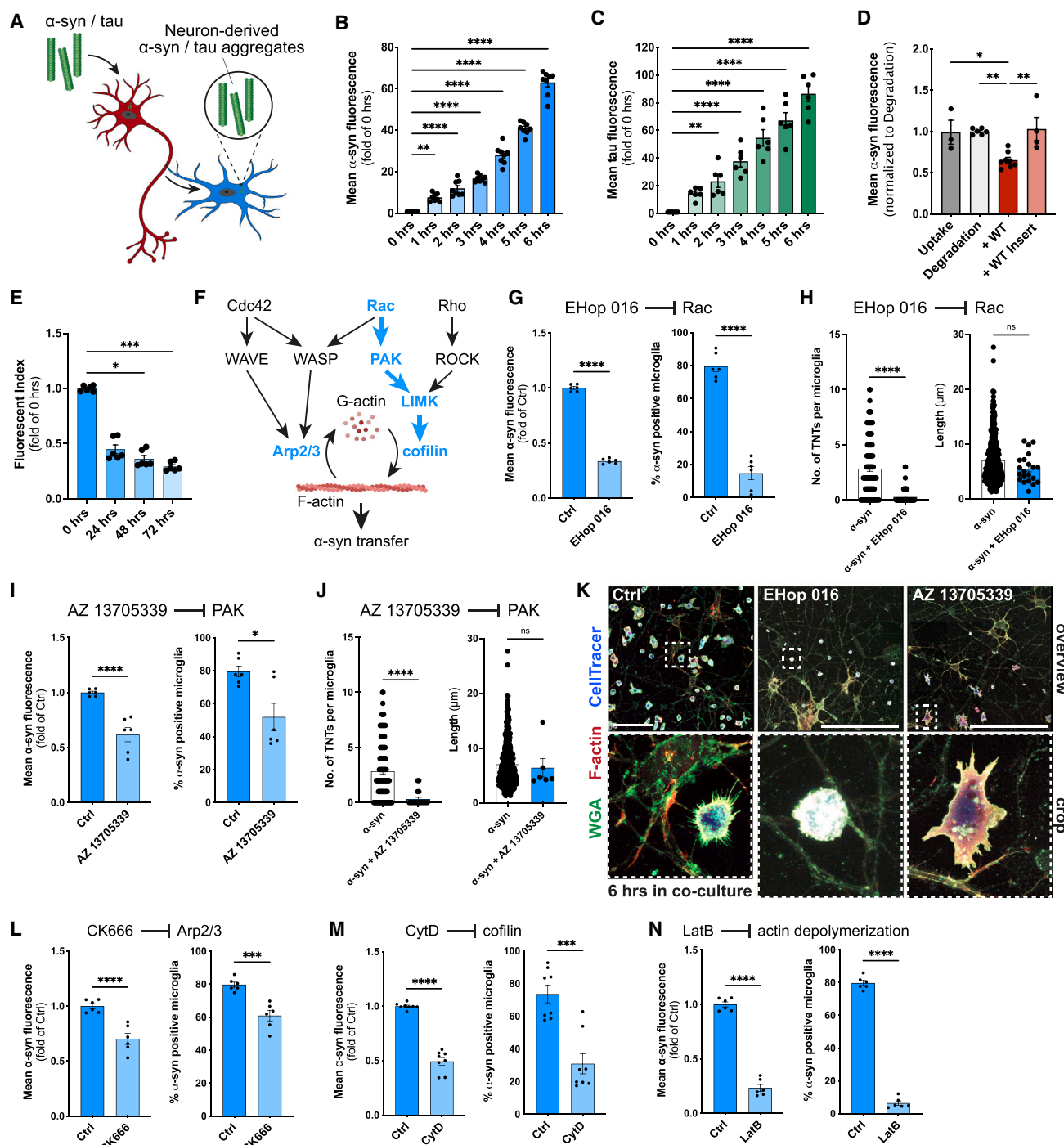


Figure 3. α -syn transfer is regulated by the Rac-PAK signaling pathway

(A) Schematic of α -syn and tau aggregate transfer from neurons to microglia.
 (B) Transfer of α -syn aggregates from neurons to microglia. $n = 4$, $N = 8$. $^{**}p = 0.006$, $^{****}p < 0.0001$.
 (C) Transfer of tau aggregates from neurons to microglia. $n = 3$, $N = 6$. $^{**}p = 0.006$, $^{****}p < 0.0001$.
 (D) α -syn levels in primary neurons conducted after the uptake of α -syn (Uptake) or after cultivating them for 24 h without (Degradation) or with primary microglia (WT), allowing direct neuron-microglia contact, or not, due to a transwell insert (WT insert). $n = 3$, $N = 3$ for phagocytosis, $N = 6$ for degradation, $N = 8$ (+WT), $N = 4$ (+WT insert). $^{*}p = 0.0283$, $^{**}p = 0.0044$ (Degradation vs. +WT), $^{**}p = 0.0064$ (+WT vs. +WT insert).
 (E) Fate of neuron-derived α -syn aggregates in microglia over time. $n = 3$, $N = 6$. $^{*}p = 0.0197$, $^{***}p = 0.0003$.
 (F) Schematic of F-actin remodeling by GTPases and downstream effectors.
 (G) α -syn transfer using the Rac inhibitor EHOP016 (1 μ M, 6 h). $n = 3$, $N = 6$. $^{****}p < 0.0001$.

(legend continued on next page)

the mouse cerebral cortex from the Machine Intelligence from Cortical Networks (MICrONS) Consortium dataset.⁴⁷ We found open-ended tubular connections between neurons and microglia resembling TNTs (TNT-like) (Figures 4C, S4A, and S4B). Immunostainings of *ex vivo* organotypic slice cultures (Figures S4C and S4D), murine models of PD and FTD (Figures S5A–S5E), and postmortem human brain tissue from healthy donors and patients with AD or dementia with Lewy bodies (DLB) (Figures S5F–S5H) confirmed numerous TNT-like contacts between neurons and microglia. These structures were strongly P2Y12R positive, with Iba1 immunoreactivity dimly visible, and showed no diameter differences between species (Figures S5I–S5M), highlighting P2Y12R's role in TNT formation. Our data suggest that TNT formation between neurons and microglia occurs *in vivo* in mice and humans. However, further research is needed to conclusively characterize these connections as TNTs in both structure and function.

Microglia restore neuronal network activity and functioning

The accumulation of α -syn in neurons is linked to decreased neuronal network activity in a DLB transgenic mouse model,⁴⁸ while tau impairs neuronal circuits in AD models.⁴⁹ We investigated if microglial removal of aggregates and mitochondrial support could improve α -syn- and tau-induced neuronal network disturbances by assessing Ca^{2+} oscillations in neurons expressing GCaMP6f. Co-culturing naive neurons with microglia for 6 h did not affect neuronal network activity (Figure S6A). However, loading neurons with α -syn reduced the frequency of Ca^{2+} transients (Figure 4D). Importantly, co-incubation with microglia restored the α -syn-suppressed Ca^{2+} oscillation frequency when physical contact was permitted (Figure 4D), with similar results for tau (Figure 4E). To further substantiate these findings, we performed single patch-clamp experiments (Figures 4F–4H) and confirmed that α -syn aggregation reduced burst frequency (Figures 4F and 4G). These effects were reproduced under current-clamp conditions (Figure S6B). Importantly, co-incubation of neurons with microglia reversed these effects (Figures 4F and 4G), with a slight charge reduction (Figure 4H). No benefit was seen when physical contact was prevented (Figure S6C). An α -amino-3-hydroxy-5-methyl-4-isoxazolepropionic acid (AMPA) receptor antagonist confirmed that burst discharges were driven by glutamatergic synaptic transmission (Figure S6D). These findings suggest that microglial TNTs, by relieving α -syn or tau aggregates from neurons, reduce neuronal ROS levels and directly support neuronal function and integrity.

Microglia rescue neurons from cellular impairment by the donation of functional mitochondria

TNTs are essential for mitochondrial transport between cells.^{50,51} For example, cancer cells can acquire mitochondria from immune cells to support their metabolism.⁵² We labeled microglial mitochondria with MitoTracker and found that microglia transfer mitochondria to neurons loaded with pathogenic proteins via free-floating TNTs (Figures 5A–5C and S6E–S6G and Video S2). This process requires direct contact between microglia and neurons and results in the integration of microglial mitochondria into the neuronal network (Figure S6F). Mitochondria transfer was primarily from microglia to neurons, with minimal movement in the opposite direction (Figure S6I). BSA loading of neurons (Figure S6J) or LPS-activated microglia (Figure S6K) did not affect this transfer. Importantly, microglial mitochondria delivery reduced ROS levels in α -syn- or tau-loaded neurons, nearly reaching control levels after 6 h, and prevented neuronal death as indicated by a reduced SYTOX signal (Figures 5E–5H). Similar to the aggregate transfer, we identified the P2Y12R-Rac-PAK-F-actin pathway as crucial for regulating mitochondrial delivery to neurons (Figure S6L).

We conducted next-generation RNA sequencing on neurons exposed to aggregated α -syn to explore microglial mechanisms mitigating α -syn-induced neurodegeneration. Interestingly, co-culturing α -syn-treated neurons with microglia reversed the transcriptomic changes induced by α -syn alone (Figure 5J). Specifically, genes associated with ROS production and cell death were upregulated by α -syn aggregates in neurons but were ameliorated or normalized in the presence of microglia (Figure S7). Microglia rescued α -syn-loaded neurons from oxidative stress by transferring functional mitochondria. Using single-cell fluorescent imaging, we assessed mitochondrial membrane potential in α -syn-treated neurons with or without microglia as a proxy of OxPhos integrity/mitochondrial electron transport chain (ETC) efficiency. Neurons exposed to α -syn exhibited decreased membrane potential, which was restored when co-cultured with microglia (Figure 5K). Furthermore, staining for TOM20, a marker of the mitochondrial outer membrane, revealed that α -syn induced mitochondrial fragmentation in neurons, a condition alleviated by microglial co-culture (Figure 5L). ATP measurements further supported these findings, showing that α -syn exposure reduced neuronal ATP levels, which were restored to normal by microglia co-culture (Figures S8A and S8B). These results demonstrate that microglia can mitigate α -syn-induced mitochondrial

(H) TNT formation between neurons and microglia with Rac inhibitor EHOp016 (1 μM , 6 h). Left: $n = 87$ (Ctrl) and 70 (EHOp016) individual microglia. Right: $n = 131$ (Ctrl) and 21 (EHOp016) individual TNTs. **** $p < 0.0001$.

(I) α -syn transfer using the PAK inhibitor AZ13705339 (1 μM , 6 h). $n = 3$, $N = 6$. * $p = 0.0112$ (Ctrl vs. AZ13705339), **** $p < 0.0001$.

(J) TNT formation between neurons and microglia with PAK inhibitor AZ13705339 (1 μM , 6 h). Left: $n = 87$ (Ctrl) and 19 (AZ13705339) individual microglia. Right: $n = 131$ (Ctrl) and 6 (AZ13705339) individual TNTs. **** $p < 0.0001$.

(K) Immunostaining showing Rac-PAK signaling effects on TNT formation. Scale bar, 100 μm .

(L) α -syn transfer between neurons and microglia using the Arp2/3 inhibitor CK666 (5 μM , 6 h). $n = 3$, $N = 6$. *** $p = 0.0003$ (Ctrl vs. CK666), **** $p < 0.0001$.

(M) α -syn transfer between neurons and microglia using the cofilin inhibitor cytochalasin D (CytD, 0.5 μM , 6 h). $n = 3$, $N = 6$. *** $p = 0.0001$ (Ctrl vs. CytD), **** $p < 0.0001$.

(N) α -syn transfer using the actin depolymerization inhibitor latrunculin B (LatB, 0.5 μM , 6 h). $n = 3$, $N = 6$. **** $p < 0.0001$.

Schematics were created with BioRender.com and Adobe Illustrator. All graphs are mean \pm SEM and analyzed by one-way ANOVA followed by Tukey's test (B–D), Kruskal-Wallis test followed by Dunn's test (E), or t test (G–N). See also Figures S2 and S3.

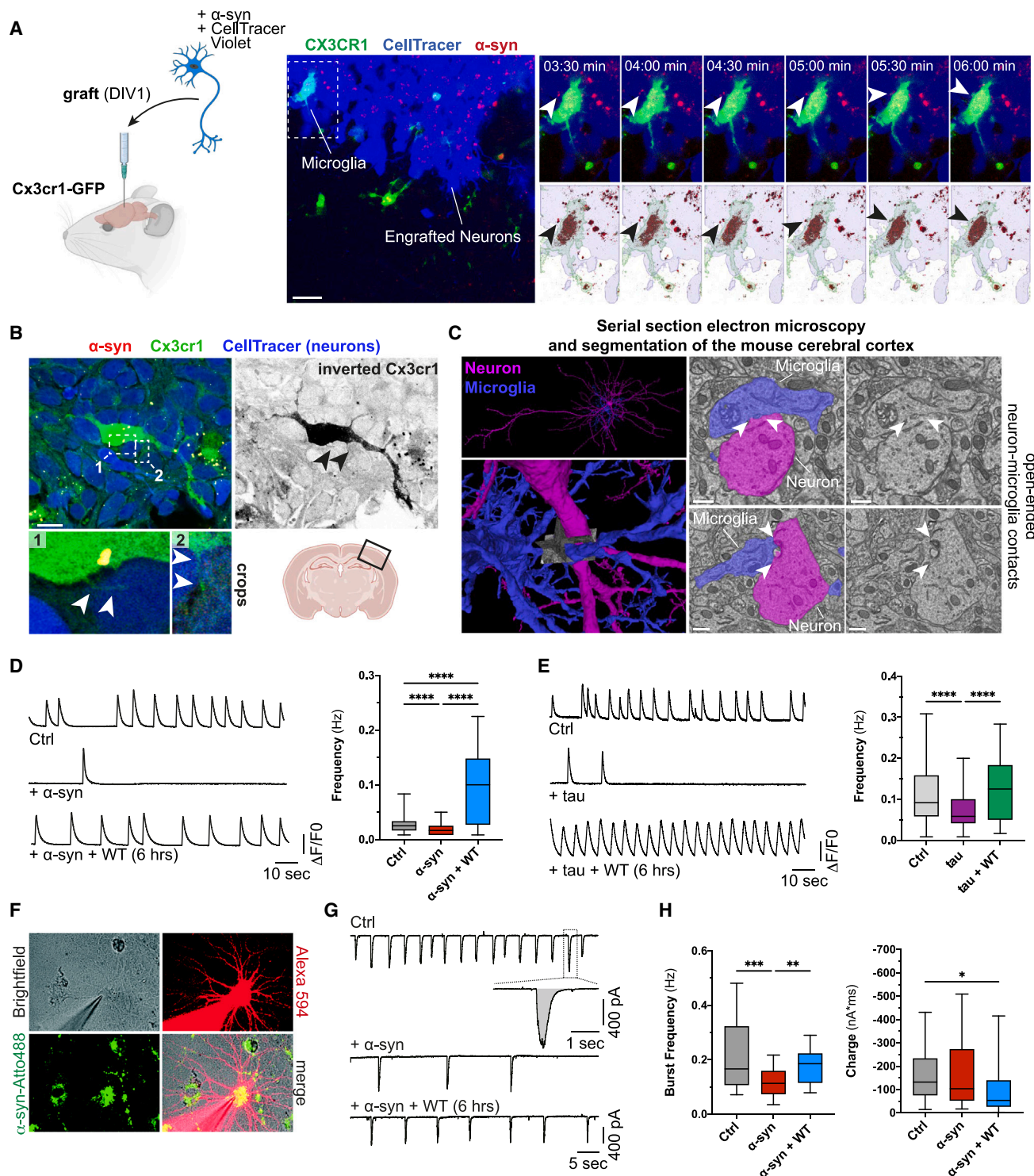


Figure 4. Microglia rescue neurons from impaired cellular functioning

(A) Schematic of *in vivo* two-photon imaging and representative recording showing neuron-microglia interactions for α -syn aggregate transfer. Scale bar, 20 μ m. (B) Immunostaining of microglia (green) connecting to α -syn-containing neurons via cellular protrusions (arrowheads). Scale bar, 10 μ m. (C) Open-ended intercellular connections (TNT-like, arrowheads) observed by serial section electron microscopy of the mouse cerebral cortex in a dataset publicly provided by the MICrONS Consortium.⁴⁷ Scale bar, 500 nm. (D) Calcium oscillations (left) and frequency quantification (right) in control neurons (Ctrl), neurons treated with α -syn aggregates (α -syn), and α -syn-treated neurons co-cultured with microglia (α -syn+WT). $n = 5$ with 65–250 individual neurons measured per condition. **** $p < 0.0001$.

(legend continued on next page)

bioenergetic deficits and preserve mitochondrial function in neurons through the transfer of functional mitochondria.

We then utilized microglia pre-treated with the mitochondrial complex III inhibitor antimycin A (AntiA) to assess the necessity of mitochondrial transfer for neuronal rescue. While AntiA did not diminish the removal of α -syn aggregates from neurons, it slightly reduced mitochondrial donation (Figures 6A and 6B). However, this partial reduction failed to rescue neurons from elevated ROS levels or prevent cell death induced by α -syn or tau (Figures 6C–6F). Consistently, AntiA-pre-treated microglia lost their ability to restore the mitochondrial membrane potential of α -syn-treated neurons and were ineffective when cell-to-cell contact was blocked using cytochalasin D (Figure 6G). Moreover, AntiA-pre-treated microglia could not restore ATP levels in α -syn-treated neurons (Figures S8A and S8B) and exacerbated the overrepresentation of genes related to OxPhos and oxidative stress in these neurons (Figure 6H). Additionally, AntiA induced an inflammatory response in microglia, exacerbating mitochondrial damage in otherwise healthy neurons (Figures S8C and S8D).

These findings underscore that neurons burdened with aggregated α -syn or tau suffer from ROS accumulation and benefit from intact mitochondrial delivery by microglia. Given the established role of oxidative stress in neurodegenerative diseases,⁵³ the TNT-mediated delivery of mitochondria to neurons may represent a novel neuroprotective mechanism of microglia.

Disease-modifying mutations fail to rescue neurons

Our data suggest that microglial TNT formation, aggregate extraction from neurons, and delivery of mitochondria to neurons are crucial physiological mechanisms. Therefore, we next investigated whether known gene variants associated with neurodegenerative diseases influence these functions (Figure 7).

Compromising microglial TNT-mediated clearance of aggregates from neurons may promote pathological aggregation within individual neurons and facilitate the rapid spread of α -syn pathology among neighboring neurons and throughout neural networks. Microglia carrying the common LRRK2 mutation *Lrrk2*(Gly2019Ser), associated with autosomal dominant and sporadic PD and DLB,⁵⁴ exhibited significantly reduced transfer of α -syn aggregates from neurons (Figures 7A and 7B) while delivering more mitochondria to neurons compared to wild-type (WT) cells (Figure 7C). Despite the increased mitochondrial delivery, LRRK2 mutant microglia failed to mitigate neuronal ROS levels and prevent cell death (Figures 7D and 7E), suggesting that mitochondria from *Lrrk2*(Gly2019Ser) mutant microglia provided less metabolic support and protection than those from WT microglia. These observations are consistent with pre-

vious findings showing metabolic dysfunction and impaired support by microglia carrying the *Lrrk2*(Gly2019Ser) mutation. Moreover, co-culturing neurons with *Lrrk2*(Gly2019Ser) microglia did not shield neurons from the α -syn-induced reduction in mitochondrial membrane potential (Figure 7F), likely due to dysfunctional mitochondria derived from LRRK2 mutant microglia.^{55,56} Importantly, using co-cultures of human induced pluripotent stem cell (iPSC)-derived neurons and microglia, including those derived from WT and LRRK2 mutant iPSCs, we observed free-floating TNTs and similar properties in α -syn aggregate and mitochondria transfer comparable to findings in murine cells (Figures 7G–7J). Notably, human iPSC-derived microglia, carrying the LRRK2 mutation, displayed deficits similar to their murine counterparts.

Next, we investigated the impact of rare coding variants in TREM2, known to increase the risk of FTD and AD,^{57,58} on microglial TNT-mediated support of neurons. Given the characteristic intraneuronal accumulation of tau in FTD and AD, we examined whether microglia carrying the *Trem2*(T66M) or *Trem2*(R47H) mutation altered the removal of aggregated tau from neurons or the delivery of mitochondria. Microglia harboring either the *Trem2*(T66M) or *Trem2*(R47H) mutation were less effective in clearing aggregated tau from neurons via TNTs (Figures 7K and 7L). However, mitochondrial delivery by microglia remained unaffected by both TREM2 mutations (Figures 7L and 7P). Nonetheless, microglia with *Trem2*(T66M) (Figures 7M and 7N) and *Trem2*(R47H) (Figures 7Q and 7R) mutations failed to alleviate neuronal ROS levels and prevent cell death.

These findings suggest that genetic variants associated with increased risk of synucleinopathies (DLB, PD) or primary (FTD) and secondary (AD) tauopathies impair microglial support of neurons by reducing TNT-mediated aggregate removal. Additionally, in the case of *Lrrk2*(Gly2019Ser), these variants also compromise the delivery of functional mitochondria.

DISCUSSION

Pathological proteins, such as α -syn and tau, are central to neurodegenerative diseases, forming insoluble aggregates within neurons that disrupt essential cellular functions and contribute to neuronal dysfunction (Figure 1). Microglia serve a critical role as the brain's surveillance and cleanup crew, actively removing abnormal extracellular protein aggregates to maintain brain homeostasis. However, microglia typically encounter these pathological proteins only after neuronal death, marking the onset of neurodegeneration. When pathological proteins remain trapped within viable neurons or sequestered in inaccessible cellular compartments, microglial clearance becomes

(E) Calcium oscillations (left) and frequency quantification (right) in control neurons (Ctrl), neurons treated with tau aggregates (tau), and tau-treated neurons co-cultured with microglia (tau+WT). $n = 3$ with 108–163 individual neurons measured per condition. **** $p < 0.0001$.

(F) Staining of a neuron exposed to α -syn aggregates analyzed by patch-clamp in co-culture with microglia.

(G) Burst frequency measured by patch-clamp in naive neurons (Ctrl), neurons treated with α -syn aggregates (α -syn), and α -syn-treated neurons co-cultured with microglia (α -syn+WT).

(H) Quantification of burst frequency and charge in untreated neurons (Ctrl), α -syn-treated neurons (α -syn), and α -syn-treated neurons co-cultured with microglia (α -syn+WT) assessed by patch-clamp. $n = 3$ with 29–42 individual neurons measured per condition. Left panel: ** $p = 0.0029$ (α -syn vs. α -syn+WT), *** $p = 0.0003$ (Ctrl vs. α -syn). Right panel: * $p = 0.0222$ (Ctrl vs. α -syn+WT).

Schematics were created with BioRender.com and Adobe Illustrator. All graphs are mean \pm SEM and analyzed by one-way ANOVA followed by Dunn's test (D–H). See also Figures S4–S6.

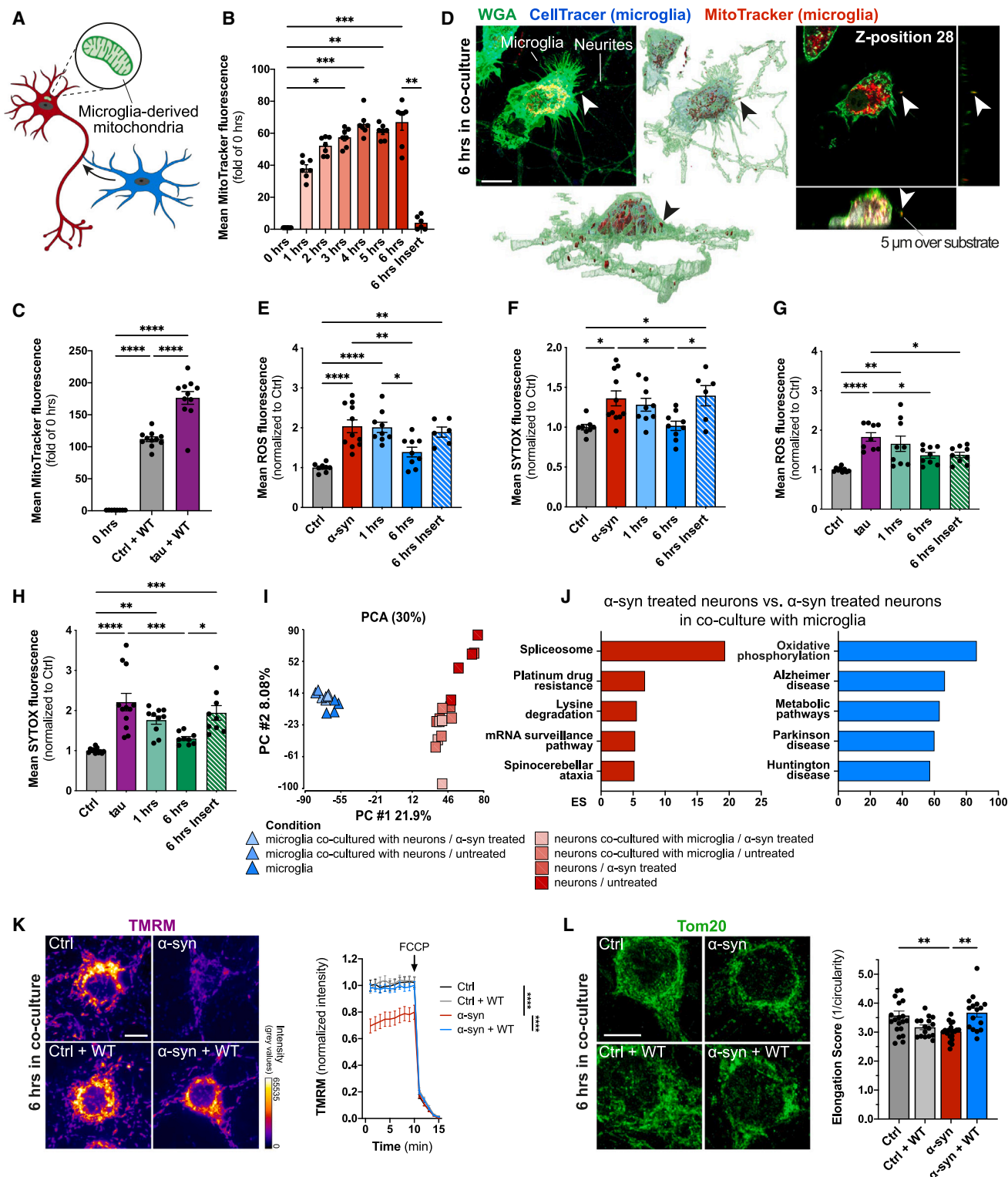


Figure 5. Microglia rescue neurons by donating mitochondria

(A) Schematic showing microglial transfer of mitochondria to neurons.

(B) Quantification of mitochondria donated by microglia to α -syn-treated neurons. $n = 4$, $N = 6$ (Ctrl, 6 h insert), $N = 7$ (1–6 h). * $p = 0.042$, ** $p = 0.0074$ (0 h vs. 5 h), *** $p = 0.0014$ (6 h vs. 6 h insert), **** $p = 0.0004$ (0 h vs. 4 h), **** $p = 0.0005$ (0 h vs. 6 h).

(C) Quantification of mitochondria donated by microglia (WT) to tau-treated neurons. $n = 3$, $N = 8$ (0 h), $N = 11$ (Ctrl+WT, tau+WT). **** $p < 0.0001$.

(legend continued on next page)

challenging. This highlights the crucial need for timely and efficient clearance mechanisms to protect neuronal health.

Microglia relieve neurons from their α -syn burden

Cytotoxic accumulations of α -syn and tau primarily afflict neurons but can also appear in glial cells as neurodegenerative diseases progress. Until recently, it was widely accepted that microglial uptake of pathological proteins was solely through phagocytosis to prevent neurodegeneration.³⁰ However, our findings challenge this view by demonstrating that microglia establish TNT connections with neurons to effectively alleviate them from cytotoxic protein burdens (Figures 2 and 3). TNTs are thin, F-actin-rich structures facilitating direct intercellular communication and material exchange, including proteins and organelles.^{40,59} They have attracted significant attention in the context of pathological protein propagation due to their role in facilitating the intercellular transmission of proteins such as α -syn and tau between neurons, astrocytes, oligodendrocytes, and pericytes. This enables the spreading of neurodegenerative pathology across different brain regions and cell types.^{16,17,19,60,61} In contrast to these studies, we recently demonstrated that microglia use TNTs to remove α -syn from interconnected burdened microglia. This capability not only promotes the health and survival of individual cells but also enhances the overall function of the microglial population, helping to mitigate inflammation and cellular dysfunction.³⁸ In accordance with the safeguarding mechanism between microglia, our presented data demonstrate that microglia, through the utilization of TNTs, play a pivotal role in the extraction of interconnected neurons from their α -syn or tau burden, resulting in the degradation of these pathological proteins in the receiving microglia (Figures 3A–3E). Very recently, a study explored TNTs connecting neurons and microglia, demonstrating efficient α -syn exchange between these cell types.³⁹ However, this study is limited in comprehensively assessing the consequences of protein exchange on cell health and survival. In contrast, our research focuses on revealing the functional outcomes of this exchange, aiming for a clearer understanding of its effects. Importantly, the study by Chakraborty et al. relied exclusively on undifferentiated cell lines labeled as neuronal, which may restrict insights into the biological implications of α -syn ex-

change between neurons and microglia.³⁹ To address this, we employed primary mouse neurons and microglia, and human iPSCs, identifying genetic risk factors crucial for microglial rescue of neurons from dysfunction in more physiologically relevant systems. This approach deepens our understanding of the intricate mechanisms in this cellular interaction, offering insights into potential therapeutic strategies for neurodegenerative conditions linked to α -syn and tau pathology.

TNT formation between neurons and microglia is regulated by Rac-PAK

Actin is crucial for TNT formation, regulated by GTPases like Rho family members (e.g., RhoA, Rac1, Cdc42) and their signaling pathways that control cytoskeletal dynamics and material exchange in various cell types.^{38,62–67} Hanna et al. demonstrated that TNT formation involves Cdc42 and Rac1, along with their effectors WASP and WAVE2.⁶² Inhibition of Rac or Cdc42 led to a significant decrease in the total number of TNTs. In keeping with this, we found that inhibition of Rac1 and its downstream effector PAK significantly reduces TNT formation and α -syn transfer between neurons and microglia (Figures 3F–3N). Rac1 and PAK are pivotal in cellular signaling, influencing cytoskeletal dynamics, cell motility, and synaptic plasticity. Their roles in neurodegenerative diseases, though complex, are increasingly recognized (for review see Marei and Malliri⁶⁸). For instance, Rac1 is associated with two genes linked to PD, affecting its normal function. On the one hand, Rac1 is ubiquitinated by parkin, a mutation associated with juvenile PD.⁶⁹ On the other hand, LRRK2, responsible for the most common familial form of PD, interacts specifically and strongly with Rac1.⁷⁰ Moreover, α -syn selectively suppresses Rac1 activation, leading to abnormal cytoskeletal rearrangements in SH-SY5Y neuronal cells.⁷¹ In light of this, PD-associated alteration in Rac1 activity may likely impact the formation and functionality of TNTs. TNTs facilitate α -syn transfer from neurons to microglia for clearance. Reduced Rac1 activity might impair this TNT-mediated clearance process, potentially leading to α -syn accumulation in PD brains. Further research is needed to fully elucidate how Rac1 activity influences TNT formation and function. Modulating Rac1 activity or its downstream pathways may provide a potential avenue for enhancing TNT formation and improving the clearance of pathological proteins such

(D) Immunostaining and 3D reconstruction of microglia-derived mitochondria (arrowheads) in TNTs connecting neurons and microglia. Scale bar, 10 μ m.

(E) ROS production in naive or α -syn-treated neurons (0.2 μ M) with or without microglia in co-culture. $n = 4$, $N = 8$ (Ctrl), $N = 11$ (α -syn), $N = 9$ (1 h, 6 h), $N = 6$ (6 h insert). * $p = 0.013$, ** $p = 0.0011$ (Ctrl vs. 6 h insert), ** $p = 0.0053$ (α -syn vs. 6 h), **** $p < 0.0001$.

(F) SYTOX signal in naive or α -syn-treated neurons (0.2 μ M) with or without microglia in co-culture. $n = 4$, $N = 8$ (Ctrl), $N = 11$ (α -syn), $N = 9$ (1 h, 6 h), $N = 6$ (6 h insert). * $p = 0.0272$ (Ctrl vs. α -syn), * $p = 0.0363$ (Ctrl vs. 6 h insert), * $p = 0.028$ (α -syn vs. 6 h), * $p = 0.0372$ (6 h vs. 6 h insert).

(G) ROS production in naive or tau-treated neurons with or without microglia in co-culture. $n = 4$, $N = 9$. * $p = 0.0378$ (tau vs. 6 h insert), * $p = 0.0369$ (tau vs. 6 h), ** $p = 0.0012$ (Ctrl vs. 1 h), **** $p < 0.0001$.

(H) SYTOX signal in naive or tau-treated neurons (0.2 μ M) with or without microglia in co-culture. $n = 4$, $N = 12$ (Ctrl, tau), $N = 10$ (1 h), $N = 9$ (6 h, 6 h insert). * $p = 0.0263$ (Ctrl vs. 6 h insert), ** $p = 0.0020$ (Ctrl vs. 1 h), *** $p = 0.0003$ (tau vs. 6 h), **** $p = 0.0002$ (Ctrl vs. 6 h insert), **** $p = 0.0001$.

(I) 2D principal component analysis (PCA) of neurons (red) and microglia (blue) under different culture conditions.

(J) Bar charts of top 5 enriched pathways for induced (red) and suppressed (blue) genes in α -syn-treated neurons after 6 h in co-culture with microglia.

(K) TMRM signal intensity in naive neurons (Ctrl), α -syn-treated neurons (α -syn), naive neurons co-cultured with microglia (Ctrl+WT), and α -syn-treated neurons co-cultured with microglia (α -syn+WT). $n = 3$, $N = 56$ cells. **** $p < 0.0001$. Scale bar, 10 μ m.

(L) Immunostaining (left) and quantification (right) of mitochondrial elongation in naive neurons (Ctrl), α -syn-treated neurons (α -syn), naive neurons co-cultured with microglia (Ctrl+WT), and α -syn-treated neurons co-cultured with microglia (α -syn+WT). $n = 3$, $N = 19$ (Ctrl, α -syn), $N = 16$ (α -syn+WT, Ctrl+WT). ** $p = 0.0067$ (Ctrl vs. α -syn), ** $p = 0.002$ (α -syn vs. α -syn+WT). Scale bar, 5 μ m.

Schematics were created with BioRender.com and Adobe Illustrator. All graphs are mean \pm SEM and analyzed by one-way ANOVA followed by Tukey's test (C–G and L), Kruskal-Wallis test followed by Dunn's test (B and H), or two-way ANOVA (K). See also Figures S6 and S7.

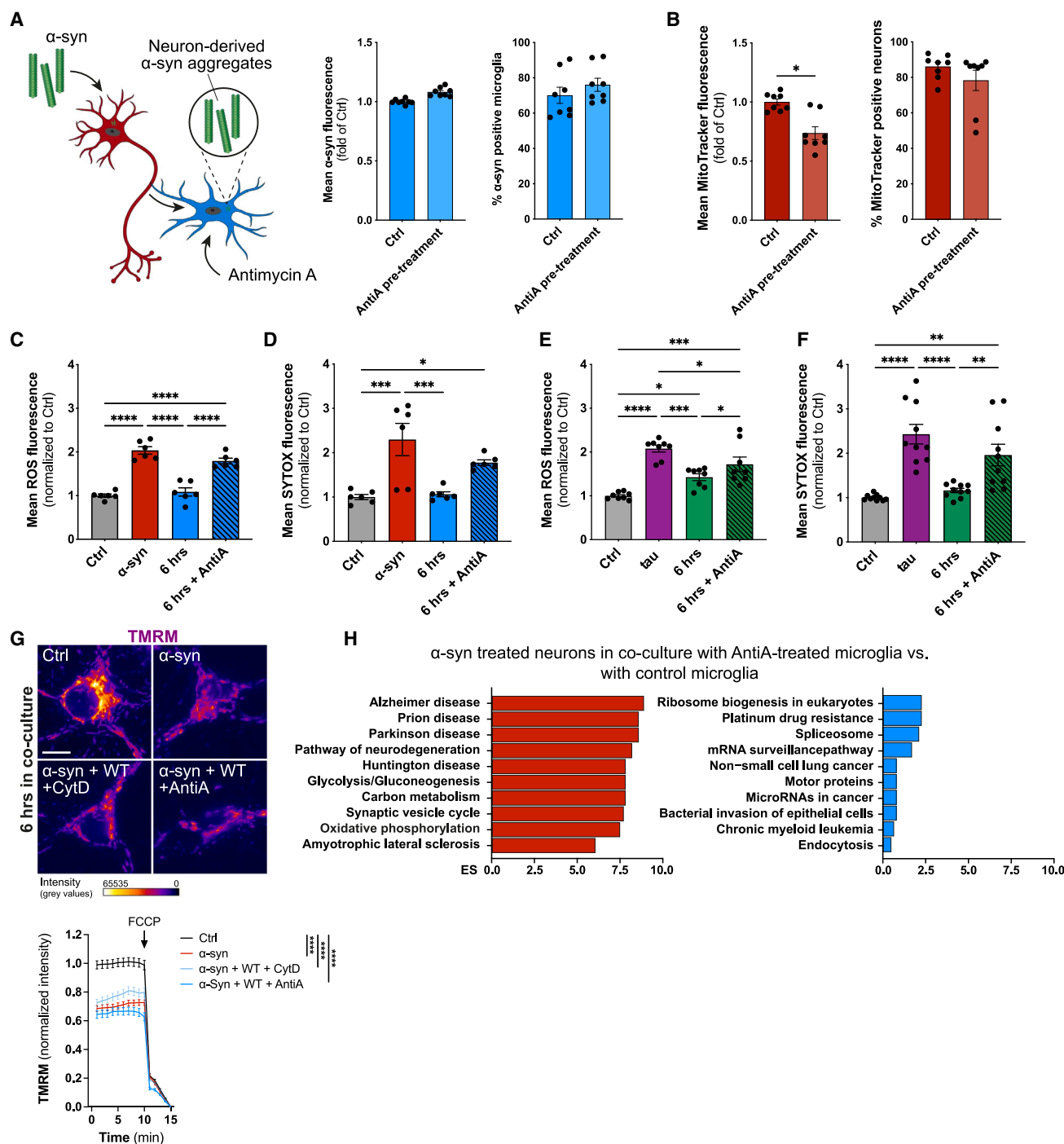


Figure 6. AntiA pre-treated microglia fail to rescue neurons from oxidative stress and cell death

(A) Schematic of experimental setup (left) used in (A)–(H) and quantification (right) of α -syn transfer to antimycin A (AntiA, 100 nM, 16 h) pre-treated microglia. $n = 3$, $N = 8$.

(B) Mitochondrial transfer from AntiA pre-treated microglia to α -syn-treated neurons. $n = 3$, $N = 8$. * $p = 0.0104$.

(C) Effects of mitochondrial donation from AntiA pre-treated microglia to α -syn loaded neurons. $n = 3$, $N = 6$. **** $p < 0.0001$.

(D) SYTOX fluorescence of naive or α -syn-treated neurons co-cultured with microglia pre-treated with AntiA. $n = 3$, $N = 6$. * $p = 0.0404$ (Ctrl vs. 6 h+AntiA), *** $p = 0.0009$ (α -syn vs. 6 h+AntiA), *** $p = 0.0005$ (Ctrl vs. α -syn).

(E) Effects of mitochondrial donation from AntiA pre-treated microglia to tau-loaded neurons. $n = 3$, $N = 8$. * $p = 0.0479$ (6 h vs. 6 h+AntiA), * $p = 0.0351$ (tau vs. 6 h+AntiA), * $p = 0.0171$ (Ctrl vs. 6 h), *** $p = 0.0003$ (tau vs. 6 h), *** $p = 0.0001$ (Ctrl vs. 6 h+AntiA), **** $p < 0.0001$ (Ctrl vs. tau).

(legend continued on next page)

as α -syn, which could result in a slowing of the progression of PD and similar neurodegenerative diseases.

TNT formation in mice and human

To validate the *in vivo* transfer of pathological proteins from neurons to microglia, we employed two-photon confocal laser scanning microscopy. Engrafting α -syn-loaded neurons into *Cx3Cr1^{GFP+/-}* mice allowed us to observe the transfer of α -syn aggregates into microglia over time (Figure 4A). However, whether this transfer occurred via TNTs remains uncertain due to visualization limitations. To further provide *in vivo* evidence for the existence of the transport of pathological proteins from neurons into microglia, we engrafted α -syn-loaded neurons into the brains of *Cx3Cr1^{GFP+/-}* mice and followed the fate of α -syn over time. Indeed, we found a transfer of α -syn aggregates from engrafted neurons into microglia (Figure 4A). Whether this transport was mediated via TNTs remains, however, unclear due to limitations in the quality of visualization. It is worth noting these experiments were conducted under artificial conditions to overcome experimental limitations and may not fully reflect the brain's actual environment. α -syn pathology primarily affects the substantia nigra and striatum, regions inaccessible to two-photon laser scanning techniques. Similarly, in Tau22 animals with tau pathology, phosphorylated tau deposits mainly occur in the hippocampus and sporadically affect neurons in the cortex.

To provide further evidence of the presence of TNTs between neurons and microglia *in vivo*, we validated the presence of TNT-like structures between neurons and microglia using publicly available electron microscopy datasets. Serial section electron microscopy of the mouse cerebral cortex from the MICrONS Consortium dataset⁴⁷ showed open-ended intercellular connections resembling TNTs (Figure 4C). Additionally, immunostaining analyses of *ex vivo* organotypic slice cultures, murine models of PD and FTD, and postmortem human brain tissues from healthy individuals and patients with AD and DLB also demonstrated intercellular connections resembling TNTs. Nevertheless, further research is required to definitively ascertain the presence of TNTs or open-ended structures between neurons and microglia in tissue, as well as their capacity to exchange pathological proteins and mitochondria.

Microglia restore neuronal function

In DLB transgenic mouse models, α -syn accumulation in neurons correlates with impaired neuronal network function,⁴⁸ whereas in AD transgenic models, tau accumulation disrupts neuronal circuits.⁴⁹ We observed that both α -syn and tau within neurons reduced basal neuronal network frequency, as indicated by Ca^{2+} oscillation and electrophysiological recordings

(Figures 4D–4H). Remarkably, co-incubation of neurons with microglia reversed this suppression of neuronal network frequency induced by pathological proteins, contingent upon direct physiological contact between neurons and microglia.

Recent studies have highlighted bidirectional communication between neuronal activity and microglia responses.^{72–74} Microglia not only react to changes in neuronal activity but can also actively modulate neuronal activity upon contact.^{74–77} This suggests that microglial TNT formation, along with the transfer of α -syn or tau aggregates from neurons to microglia and the delivery of mitochondria to neurons, likely influences neuronal function directly. By aiding in the clearance of intraneuronal debris and supporting metabolic health, microglial TNTs contribute to the maintenance of neuronal function and integrity.

Mitochondrial donation attenuates oxidative stress in neurons

Mitochondrial dysfunction is a critical factor underlying several neurodegenerative diseases such as AD, PD, and FTD. This dysfunction results in energy deficits, heightened oxidative stress, impaired calcium regulation, and disrupted signaling pathways, all contributing to cellular damage and death. Neurons, with their high energy demands, are particularly vulnerable to mitochondrial defects. Consequently, disruptions in mitochondrial health can profoundly impact neuronal function and survival.⁷⁸ For instance, impaired OxPhos can lead to excessive ROS production, exacerbating mitochondrial damage and ultimately contributing to neuronal death.⁷⁹ Here, we observed that both α -syn and tau impair mitochondrial function, evidenced by decreased OxPhos, increased oxidative stress, and elevated cell death (Figure 1). Remarkably, co-culture of affected neurons with microglia resulted in the transfer of healthy mitochondria from microglia to neurons, effectively restoring mitochondrial function and preserving neuronal health (Figure 5). The process of TNT-mediated mitochondrial donation has attracted significant interest for its potential to mitigate mitochondrial dysfunction in cells experiencing impaired energy production and heightened oxidative damage.^{80–86}

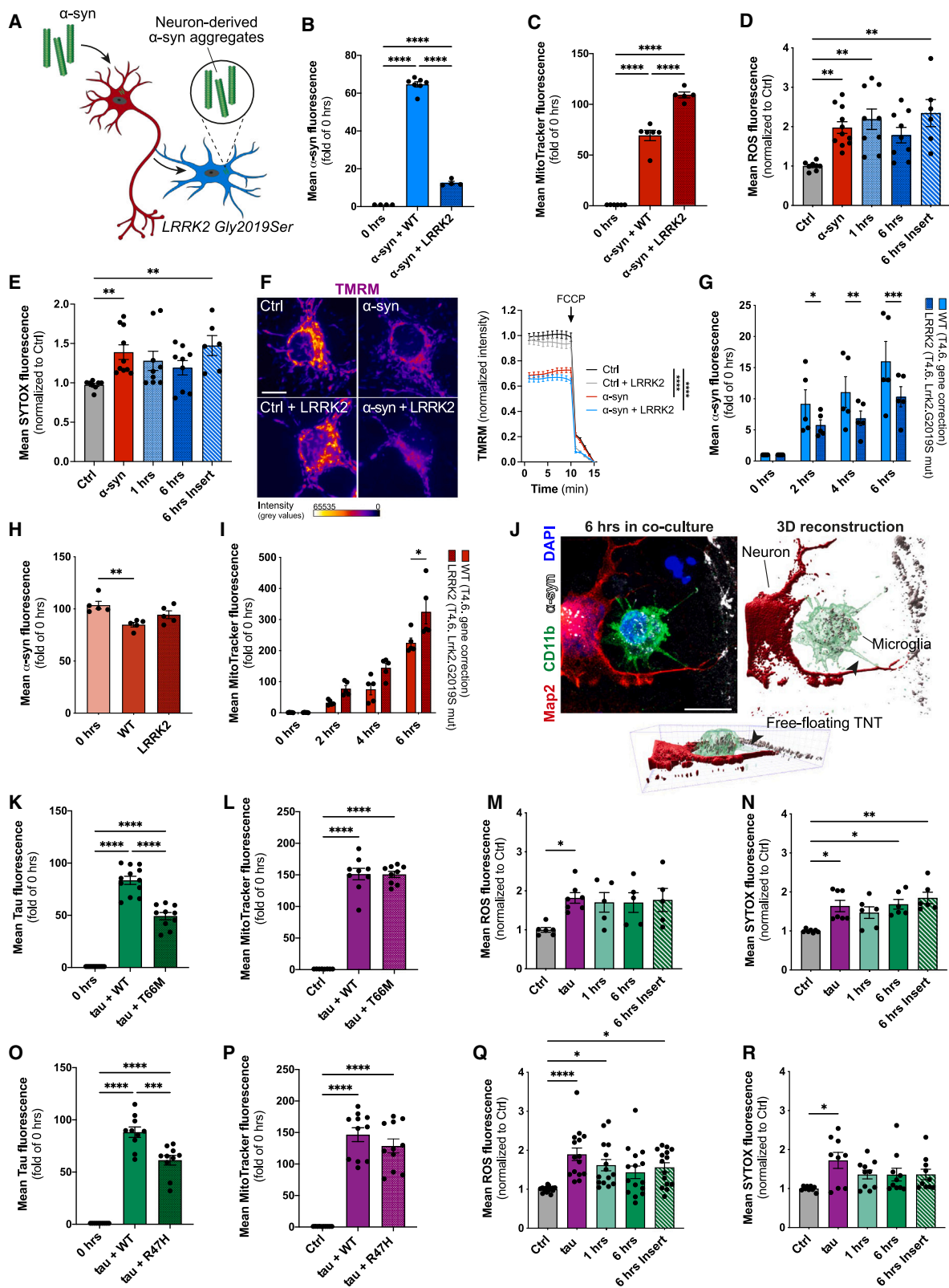
Our previous research has shown that mitochondria can be horizontally transferred between interconnected microglia, serving as a rescue mechanism to alleviate inflammation and prevent cell death.³⁸ To convincingly demonstrate the efficacy of mitochondrial donation in restoring neuronal mitochondrial function, we conducted proof-of-principle experiments using microglia with impaired mitochondria due to AntiA pre-treatment, which irreversibly destroys mitochondrial function. These impaired microglia failed to alleviate oxidative stress and mitochondrial dysfunction in neurons (Figure 6), highlighting the

(F) SYTOX fluorescence of naive or tau-treated neurons co-cultured with microglia pre-treated with AntiA. $n = 3$, $N = 10$. ** $p = 0.0085$ (6 h vs. 6 h+AntiA), ** $p = 0.0013$ (Ctrl vs. 6 h+AntiA), **** $p < 0.0001$.

(G) Immunostaining (upper panel) and analysis (lower panel) of TMRM signal in naive neurons (Ctrl), α -syn-treated neurons (α -syn), α -syn-treated neurons co-cultured with microglia treated with CytD (α -syn+WT+CytD), and α -syn-treated neurons co-cultured with AntiA pre-treated microglia (α -syn+WT+AntiA). $n = 4$, $N = 79$ (Ctrl), $N = 88$ (α -syn), $N = 89$ (α -syn+WT+CytD), $N = 58$ (α -syn+WT+AntiA). **** $p < 0.0001$. Scale bar, 10 μm .

(H) Bar charts of top 10 enriched pathways for induced (red) and suppressed (blue) genes in α -syn-treated neurons co-cultured with AntiA pre-treated microglia compared to α -syn-treated neurons co-cultured with control microglia.

Schematics were created with BioRender.com and Adobe Illustrator. All graphs are mean \pm SEM and analyzed by t test (A and B), one-way ANOVA followed by Tukey's test (C–F), or two-way ANOVA (G). See also Figure S8.



(legend on next page)

critical role of mitochondrial donation in preserving neuronal function. This aligns with existing research focused on rescuing damaged cells,^{82–84} emphasizing the significance of maintaining mitochondrial quality to prevent oxidative damage propagation. Of note, co-culturing impaired mitochondria-containing microglia with untreated neurons propagates oxidative stress to previously healthy neurons, indicating that introducing compromised mitochondria can harm beyond the initially affected cells. This underscores the importance of preserving mitochondrial quality to prevent oxidative damage spread and emphasizes the need for strategies promoting healthy mitochondria transfer to mitigate these effects.

Disease-modifying mutations impair TNT-based rescue of burdened neurons

Compromising microglial TNT-based clearance of aggregates from neurons may accelerate pathological aggregation within individual neurons and facilitate faster spread of α -syn pathology between neighboring neurons and across networks. Thus, to explore the impact of disease-modifying mutations on these TNT-based rescue mechanisms, we utilized microglia carrying relevant mutations.

The *Gly2019Ser* mutation in *Lrrk2* is a prevalent genetic cause of PD and DLB.⁵⁴ Microglia carrying this mutation show reduced ability to extract α -syn aggregates from neurons, yet they deliver more mitochondria to neurons compared to WT cells in both primary murine microglia (Figures 7A–7C) and human iPSC-derived microglia (Figures 7G–7I). Despite increased mitochondria delivery, LRRK2 mutant microglia fail to reduce neuronal ROS levels and cell death (Figures 7D–7F), indicating diminished metabolic support and protective capacity. These findings corroborate previous observations of mitochondrial impairment^{55,56} and reduced support to neighboring cells by microglia with the

Lrrk2(*Gly2019Ser*) mutation.³⁸ Recent studies show that the *Lrrk2*(*Gly2019Ser*) mutation inhibits α -syn degradation in PD models^{87,88} and disrupts mitochondrial depletion through mitophagy.⁸⁹ Moreover, pathogenic mutations in LRRK2 enhance pro-inflammatory responses,⁹⁰ potentially reducing microglial clearance capacity for protein aggregates and promoting cytotoxic protein accumulation.³²

Rare coding variants of the *Trem2* gene, such as *Trem2*(*T66M*) and *Trem2*(*R47H*), increase the risk of developing FTD and AD.^{57,58} Microglia carrying these mutations showed reduced efficiency in clearing aggregated tau from neurons via TNTs, while mitochondrial delivery remained unaffected compared to WT cells (Figures 7K–7R). However, microglia with *Trem2* mutations failed to reduce neuronal ROS levels and cell death. Recent studies have demonstrated that *Trem2* missense mutations, including *R47H* and *T66M*, impair cell movement and uptake of substrates in iPSC-derived microglia,⁹¹ and lead to significant metabolic deficits such as reduced mitochondrial respiratory capacity.⁹² *R47H* mutant microglia are also hyper-responsive to inflammatory stimuli, potentially affecting their overall function.⁹¹

These findings indicate that gene variants linked to increased risk for synucleinopathies (DLB, PD) or primary (FTD) and secondary (AD) tauopathies disrupt microglial support of neurons by impairing TNT-mediated protection mechanisms. Specifically, compromised clearance of pathological proteins, mitochondrial dysfunction, and impaired mitophagy may collectively contribute to the failure of rescuing neurons in PD and FTD associated with these mutations, thereby promoting inflammation and cellular dysfunction in neurodegenerative diseases.

Limitations of the study

In conclusion, our findings suggest that the accumulation of pathological protein aggregates within neurons triggers the

Figure 7. Disease-associated gene variants fail to rescue neurons from oxidative stress and cell death

- (A) Schematic of α -syn transfer from neurons to *Lrrk2*(*Gly2019Ser*) microglia.
- (B) Quantification of α -syn transfer to LRRK2 mutant microglia. $n = 3$, $N = 4$ (0 h, α -syn+LRRK2), $N = 7$ (α -syn+WT). **** $p < 0.0001$.
- (C) Quantification of mitochondria transfer from LRRK2 mutant microglia to α -syn-treated neurons. $n = 5$, $N = 6$ (0 h, α -syn+WT), $N = 5$ (α -syn+LRRK2). **** $p < 0.0001$.
- (D) Effects of LRRK2 mutant microglia on ROS production in α -syn-treated neurons. $n = 4$, $N = 8$ (Ctrl); $N = 11$ (α -syn), $N = 9$ (1 h, 6 h), $N = 6$ (6 h insert). ** $p = 0.0099$ (Ctrl vs. α -syn), ** $p = 0.002$ (Ctrl vs. 1 h), ** $p = 0.0016$ (Ctrl vs. 6 h insert).
- (E) LRRK2 mutant microglia effect on SYTOX intercalation in α -syn-treated neurons. $n = 4$, $N = 8$ (Ctrl), $N = 10$ (α -syn), $N = 9$ (1 h, 6 h), $N = 6$ (6 h insert). ** $p = 0.0094$ (Ctrl vs. 6 h insert), ** $p = 0.0069$ (Ctrl vs. α -syn).
- (F) TMRM signal in Ctrl neurons (Ctrl), α -syn neurons (α -syn), naive neurons in co-culture with LRRK2 microglia (Ctrl+LRRK2), and α -syn-treated neurons in co-culture with LRRK2 microglia (α -syn+LRRK2). $n = 4$, $N = 79$ (Ctrl), $N = 88$ (α -syn), $N = 44$ (Ctrl+LRRK2), $N = 55$ (α -syn+LRRK2). **** $p < 0.0001$. Scale bar, 10 μ m.
- (G) α -syn transfer from iPSC-derived neurons to WT or mutant *Lrrk2*.G2019S microglia. $n = 3$, $n = 5$. * $p = 0.0482$, ** $p = 0.0098$, *** $p = 0.0006$.
- (H) α -syn content in iPSC-derived neurons co-cultured with WT or mutant *Lrrk2*.G2019S microglia. $n = 3$, $n = 5$. ** $p = 0.0047$.
- (I) Mitochondria transfer from WT or mutant *Lrrk2*.G2019S microglia to iPSC-derived neurons. $n = 3$, $n = 5$. * $p = 0.0253$.
- (J) Immunostaining and 3D reconstruction of microglia-neuron interactions via TNTs. Scale bar, 10 μ m.
- (K) Tau transfer to *Trem2*(*T66M*) microglia. $n = 4$, $N = 12$ (0 h, tau+WT), $N = 10$ (tau+T66M). **** $p < 0.0001$.
- (L) Mitochondria transfer from *Trem2*(*T66M*) microglia to neurons. $n = 3$, $N = 9$. **** $p < 0.0001$.
- (M) *Trem2*(*T66M*) microglia effect on ROS production in tau-treated neurons. $n = 3$, $N = 5$ (1 h, 6 h, 6 h insert), $N = 6$ (Ctrl), $N = 7$ (tau). * $p = 0.0364$.
- (N) *Trem2*(*T66M*) microglia effect on SYTOX intercalation in tau-treated neurons. $n = 3$, $N = 6$ (1 h, 6 h, 6 h insert), $N = 7$ (Ctrl, tau). * $p = 0.0438$ (Ctrl vs. tau), * $p = 0.0207$ (Ctrl vs. 6 h), ** $p = 0.0014$ (Ctrl vs. 6 h insert).
- (O) Tau transfer to *Trem2*(*R47H*) microglia. $n = 4$, $N = 10$. **** $p = 0.0001$ (tau+WT vs. tau+R47H), **** $p < 0.0001$.
- (P) Mitochondria transfer from *Trem2*(*R47H*) microglia to neurons. $n = 3$, $N = 14$ (Ctrl), $N = 11$ (tau+WT, tau+R47H). **** $p < 0.0001$.
- (Q) *Trem2*(*R47H*) microglia effect on ROS production in tau-treated neurons. $n = 3$, $N = 15$. * $p = 0.0292$ (Ctrl vs. 6 h insert), * $p = 0.0124$ (Ctrl vs. 1 h), **** $p < 0.0001$ (Ctrl vs. tau).
- (R) *Trem2*(*R47H*) microglia effect on SYTOX intercalation in tau-treated neurons. $n = 3$, $N = 9$ (Ctrl, tau), $N = 10$ (1 h, 6 h, 6 h insert). * $p = 0.0109$ (Ctrl vs. tau). Schematics by BioRender.com and Adobe Illustrator. Graphs: mean \pm SEM, analyzed by ANOVA (B–D, F, H, K–M, and O–R), Kruskal-Wallis (E and N), or two-way ANOVA (G and I).

formation of TNTs between microglia and neurons. These TNTs facilitate the exchange of proteins and mitochondria, crucial for promoting neuronal survival under conditions of protein accumulation. Enhancing the stabilization or activation of TNT-mediated transfer and subsequent microglial degradation of pathological proteins may help mitigate disease progression in neurodegenerative disorders characterized by intraneuronal protein aggregation.

However, this study has limitations that warrant further investigation. We did not thoroughly explore the cellular mechanisms underlying the formation of membrane structures facilitating α -syn and mitochondrial transfer, including membrane contact formation, fusion dynamics, cargo selectivity, and directionality. While we demonstrated α -syn exchange *in vivo*, definitive confirmation of TNT-mediated transfer remains elusive. The fragility of TNTs and challenges in their visualization via two-photon microscopy *in vivo* raise uncertainties about their persistence and observation. Current literature on TNTs in the CNS *in vivo*^{93,94} is limited, underscoring the need for additional research to fully comprehend these complex cellular interactions and molecular processes governing protein and mitochondrial transport between neurons and microglia, both *in vitro* and *in vivo*.

STAR★METHODS

Detailed methods are provided in the online version of this paper and include the following:

- KEY RESOURCES TABLE
- RESOURCE AVAILABILITY
 - Lead contact
 - Materials availability
 - Data and code availability
- EXPERIMENTAL MODELS AND SUBJECT DETAILS
 - Ethical considerations
 - Animal procedures and sample collection
 - Human tissue samples
 - Primary neuronal cultures
 - Primary microglia cultures
 - Organotypic brain slice cultures (OSCs)
 - iPSC maintenance and differentiation
- METHOD DETAILS
 - Antibodies and reagents
 - Immunohistochemical staining
 - Immunocytochemistry
 - Electron microscopy
 - Recombinant α -syn preparation
 - Recombinant tau preparation
 - α -syn, tau, and mitochondria transfer experiments
 - Electrophysiology
 - Calcium imaging
 - Live cell imaging
 - ROS release and SYTOX staining
 - Oxygen consumption rate assessment
 - Imaging and mitochondrial analysis
 - TMRM measurements
 - ATP measurements
 - RNA sequencing analysis
 - Cranial window placement and intracranial engraftment of primary cortical neurons
 - *In vivo* two-photon imaging
- QUANTIFICATION AND STATISTICAL ANALYSIS

SUPPLEMENTAL INFORMATION

Supplemental information can be found online at <https://doi.org/10.1016/j.neuron.2024.06.029>.

ACKNOWLEDGMENTS

This work was supported by funding from the Gemeinnützige Hertie-Stiftung (P1200007) and the Alzheimer Forschung Initiative e.V. (#23002R) to H.S.; the Deutsche Forschungsgemeinschaft (DFG, German Research Foundation) under Germany's Excellence Strategy (EXC2151-390873048) to H.S., M.T.H., and E.L.; the Fonds National de la Recherche within the PEARL program (FNR/16745220) to M.T.H.; and Fondation pour la Recherche Médicale (contract ALZ201912009776) to R.M. The authors acknowledge Kevin Küpper for developing an ImageJ calcium imaging tool and Paulina Geck for creating a MatLab calcium imaging tool for data analysis. They are grateful to Prof. Gerhard Fritz and Dr. Christian Henninger from Heinrich Heine University Düsseldorf for providing Rac1^{flox/flox} mice. Special thanks to Maike Kreutzenbeck and Ulrike Stube for their assistance in the lab with RNA isolation and preparation for sequencing. The authors also thank the DZNE light microscope facility (LMF) for microscope access and advice, the DZNE Image and Data Analysis Facility (IDAF) for analysis computers and software, the Flow Cytometry Core Facility for cell sorting assistance, and the NGS Core Facility of the University Hospital Bonn for library preparation and sequencing data generation. Lastly, they acknowledge the FACS & Imaging Core Facility of the Max-Planck-Institute for Biology of Ageing for providing microscopes, flow cytometers, and support.

AUTHOR CONTRIBUTIONS

H.S. and M.T.H. designed the experiments; H.S. and F.E. performed and analyzed the cell culture and slice culture experiments with the assistance of C.G., S.O., S.C.-G., and S.S.; L.W. and D.B. performed and analyzed mitochondria assessment analysis; K.J. and H.-C.P. performed and analyzed the electrophysiology data; S.V.S., A.O., J.S., E.G., and E.L. performed and analyzed the RNA-seq data; J.L. performed scanning electron microscopy; T.B. and R.M. generated fibrillar α -syn; C.C., B.P., and A.D. performed and analyzed confocal and electron microscopy of mouse and human tissue; D.A.D.M. donated tissue samples; I.B. and R.K. generated iPSC-derived neurons and microglia; and M.T.H. and H.S. wrote the manuscript with input from all co-authors.

DECLARATION OF INTERESTS

E.L. is a co-founder and advisor at IFM Therapeutics, and M.T.H. serves as an advisory board member at IFM Therapeutics, T3D, and Alector.

DECLARATION OF GENERATIVE AI AND AI-ASSISTED TECHNOLOGIES IN THE WRITING PROCESS

During the preparation of this work, the authors used the DeepL Write tool in order to check for grammatical correctness and to improve readability. After using this tool, the authors reviewed and edited the content as needed and take full responsibility for the content of the publication.

Received: October 26, 2023

Revised: February 12, 2024

Accepted: June 28, 2024

Published: July 25, 2024

REFERENCES

1. Shrivastava, A.N., Redeker, V., Fritz, N., Pieri, L., Almeida, L.G., Spolidoro, M., Liebmann, T., Bousset, L., Renner, M., Lena, C., et al. (2015). α -synuclein assemblies sequester neuronal α 3-Na⁺/K⁺-ATPase and impair Na⁺ gradient. *EMBO J.* 34, 2408–2423. <https://doi.org/10.15252/embj.201591397>.

2. DeWitt, D.C., and Rhoades, E. (2013). α -Synuclein Can Inhibit SNARE-Mediated Vesicle Fusion through Direct Interactions with Lipid Bilayers. *Biochemistry* 52, 2385–2387. <https://doi.org/10.1021/bi4002369>.
3. Faustini, G., Bono, F., Valerio, A., Pizzi, M., Spano, P., and Bellucci, A. (2017). Mitochondria and α -Synuclein: Friends or Foes in the Pathogenesis of Parkinson's Disease? *Genes* 8, 377. <https://doi.org/10.3390/genes8120377>.
4. Griboaud, S., Tixador, P., Bousset, L., Fenyi, A., Lino, P., Melki, R., Peyrin, J.-M., and Perrier, A.L. (2019). Propagation of α -Synuclein Strains within Human Reconstructed Neuronal Network. *Stem Cell Rep.* 12, 230–244. <https://doi.org/10.1016/j.stemcr.2018.12.007>.
5. Martínez, J.H., Fuentes, F., Vanasco, V., Alvarez, S., Alaimo, A., Cassina, A., Coluccio Leskow, F., and Velazquez, F. (2018). Alpha-synuclein mitochondrial interaction leads to irreversible translocation and complex I impairment. *Arch. Biochem. Biophys.* 651, 1–12. <https://doi.org/10.1016/j.abb.2018.04.018>.
6. Cooper, A.A., Gitler, A.D., Cashikar, A., Haynes, C.M., Hill, K.J., Bhullar, B., Liu, K., Xu, K., Strathearn, K.E., Liu, F., et al. (2006). Alpha-synuclein blocks ER-Golgi traffic and Rab1 rescues neuron loss in Parkinson's models. *Science* 313, 324–328. <https://doi.org/10.1126/science.1129462>.
7. Thayanidhi, N., Helm, J.R., Nycz, D.C., Bentley, M., Liang, Y., and Hay, J.C. (2010). Alpha-synuclein delays endoplasmic reticulum (ER)-to-Golgi transport in mammalian cells by antagonizing ER/Golgi SNAREs. *Mol. Biol. Cell* 21, 1850–1863. <https://doi.org/10.1091/mbc.e09-09-0801>.
8. Flavin, W.P., Bousset, L., Green, Z.C., Chu, Y., Skarpathiotis, S., Chaney, M.J., Kordower, J.H., Melki, R., and Campbell, E.M. (2017). Endocytic vesicle rupture is a conserved mechanism of cellular invasion by amyloid proteins. *Acta Neuropathol.* 134, 629–653. <https://doi.org/10.1007/s00401-017-1722-x>.
9. Martinez-Vicente, M., and Vila, M. (2013). Alpha-synuclein and protein degradation pathways in Parkinson's disease: A pathological feedback loop. *Exp. Neurol.* 247, 308–313. <https://doi.org/10.1016/j.expneurol.2013.03.005>.
10. Alonso, A. del C., Zaidi, T., Grundke-Iqbal, I., and Iqbal, K. (1994). Role of abnormally phosphorylated tau in the breakdown of microtubules in Alzheimer disease. *Proc. Natl. Acad. Sci. USA* 91, 5562–5566.
11. Cowan, C.M., Bossing, T., Page, A., Shepherd, D., and Mudher, A. (2010). Soluble hyper-phosphorylated tau causes microtubule breakdown and functionally compromises normal tau in vivo. *Acta Neuropathol.* 120, 593–604.
12. Di, J., Cohen, L.S., Corbo, C.P., Phillips, G.R., El Idrissi, A., and Alonso, A.D. (2016). Abnormal tau induces cognitive impairment through two different mechanisms: synaptic dysfunction and neuronal loss. *Sci. Rep.* 6, 20833. <https://doi.org/10.1038/srep20833>.
13. Clavaguera, F., Bolmont, T., Crowther, R.A., Abramowski, D., Frank, S., Probst, A., Fraser, G., Stalder, A.K., Beibel, M., Staufenbiel, M., et al. (2009). Transmission and spreading of tauopathy in transgenic mouse brain. *Nat. Cell Biol.* 11, 909–913.
14. De Calignon, A., Polydoro, M., Suárez-Calvet, M., William, C., Adamowicz, D.H., Kopeikina, K.J., Pittstick, R., Sahara, N., Ashe, K.H., Carlson, G.A., et al. (2012). Propagation of tau pathology in a model of early Alzheimer's disease. *Neuron* 73, 685–697.
15. Wang, Y., Balaji, V., Kaniyappan, S., Krüger, L., Irsen, S., Tepper, K., Chandupatla, R., Maetzler, W., Schneider, A., Mandelkow, E., and Mandelkow, E.M. (2017). The release and trans-synaptic transmission of Tau via exosomes. *Mol. Neurodegener.* 12, 5. <https://doi.org/10.1186/s13024-016-0143-y>.
16. Tardivel, M., Bégard, S., Bousset, L., Dujardin, S., Coens, A., Melki, R., Buée, L., and Colin, M. (2016). Tunneling nanotube (TNT)-mediated neuron-to-neuron transfer of pathological Tau protein assemblies. *Acta Neuropathol. Commun.* 4, 117. <https://doi.org/10.1186/s40478-016-0386-4>.
17. Zhang, K., Sun, Z., Chen, X., Zhang, Y., Guo, A., and Zhang, Y. (2021). Intercellular transport of Tau protein and β -amyloid mediated by tunneling nanotubes. *Am. J. Transl. Res.* 13, 12509–12522.
18. Dilsizoglu Senol, A., Samarani, M., Syan, S., Guardia, C.M., Nonaka, T., Liv, N., Latour-Lambert, P., Hasegawa, M., Klumperman, J., Bonifacino, J.S., and Zurzolo, C. (2021). α -Synuclein fibrils subvert lysosome structure and function for the propagation of protein misfolding between cells through tunneling nanotubes. *PLoS Biol.* 19, e3001287. <https://doi.org/10.1371/journal.pbio.3001287>.
19. Abounit, S., Bousset, L., Loria, F., Zhu, S., Chaumont, F., Pieri, L., Olivo-Marin, J., Melki, R., and Zurzolo, C. (2016). Tunneling nanotubes spread fibrillar α -synuclein by intercellular trafficking of lysosomes. *EMBO J.* 35, 2120–2138. <https://doi.org/10.15252/embj.201593411>.
20. Choi, Y.R., Park, S.J., and Park, S.M. (2021). Molecular events underlying the cell-to-cell transmission of α -synuclein. *FEBS J.* 364, 6593–6602. <https://doi.org/10.1111/febs.15674>.
21. Yamada, K. (2017). Extracellular tau and its potential role in the propagation of tau pathology. *Front. Neurosci.* 11, 667.
22. Yamada, K., Holth, J.K., Liao, F., Stewart, F.R., Mahan, T.E., Jiang, H., Cirrito, J.R., Patel, T.K., Hochgräfe, K., Mandelkow, E.-M., and Holtzman, D.M. (2014). Neuronal activity regulates extracellular tau in vivo. *J. Exp. Med.* 211, 387–393.
23. Lasagna-Reeves, C.A., Castillo-Carranza, D.L., Sengupta, U., Guerrero-Munoz, M.J., Kiritoshi, T., Neugebauer, V., Jackson, G.R., and Kayed, R. (2012). Alzheimer brain-derived tau oligomers propagate pathology from endogenous tau. *Sci. Rep.* 2, 700.
24. Ferreira, N., Gonçalves, N.P., Jan, A., Jensen, N.M., Van Der Laan, A., Mohseni, S., Vægter, C.B., and Jensen, P.H. (2021). Trans-synaptic spreading of alpha-synuclein pathology through sensory afferents leads to sensory nerve degeneration and neuropathic pain. *Acta Neuropathol. Commun.* 9, 31. <https://doi.org/10.1186/s40478-021-01131-8>.
25. Schaser, A.J., Stackhouse, T.L., Weston, L.J., Kerstein, P.C., Osterberg, V.R., López, C.S., Dickson, D.W., Luk, K.C., Meshul, C.K., Woltjer, R.L., and Unni, V.K. (2020). Trans-synaptic and retrograde axonal spread of Lewy pathology following pre-formed fibril injection in an in vivo A53T alpha-synuclein mouse model of synucleinopathy. *Acta Neuropathol. Commun.* 8, 150. <https://doi.org/10.1186/s40478-020-01026-0>.
26. Colonna, M., and Butovsky, O. (2017). Microglia Function in the Central Nervous System During Health and Neurodegeneration. *Annu. Rev. Immunol.* 35, 441–468. <https://doi.org/10.1146/annurev-immunol-051116-052358>.
27. Sengupta, U., and Kaye, R. (2022). Amyloid β , Tau, and α -Synuclein aggregates in the pathogenesis, prognosis, and therapeutics for neurodegenerative diseases. *Prog. Neurobiol.* 214, 102270. <https://doi.org/10.1016/j.pneurobio.2022.102270>.
28. Pickering, M., and O'Connor, J.J. (2007). Pro-inflammatory cytokines and their effects in the dentate gyrus. In *Progress in Brain Research* (Elsevier), pp. 339–354. [https://doi.org/10.1016/S0079-6123\(07\)63020-9](https://doi.org/10.1016/S0079-6123(07)63020-9).
29. Medana, I., Martinic, M.A., Wekerle, H., and Neumann, H. (2001). Transection of Major Histocompatibility Complex Class I-Induced Neurites by Cytotoxic T Lymphocytes. *Am. J. Pathol.* 159, 809–815. [https://doi.org/10.1016/S0002-9440\(10\)61755-5](https://doi.org/10.1016/S0002-9440(10)61755-5).
30. Choi, I., Zhang, Y., Seegobin, S.P., Pruvost, M., Wang, Q., Purtell, K., Zhang, B., and Yue, Z. (2020). Microglia clear neuron-released α -synuclein via selective autophagy and prevent neurodegeneration. *Nat. Commun.* 11, 1386. <https://doi.org/10.1038/s41467-020-15119-w>.
31. Michelucci, A., Heurtaux, T., Grandbarbe, L., Morga, E., and Heuschling, P. (2009). Characterization of the microglial phenotype under specific pro-inflammatory and anti-inflammatory conditions: Effects of oligomeric and fibrillar amyloid-beta. *J. Neuroimmunol.* 210, 3–12. <https://doi.org/10.1016/j.jneuroim.2009.02.003>.

32. Scheiblich, H., Bousset, L., Schwartz, S., Griep, A., Latz, E., Melki, R., and Heneka, M.T. (2021). Microglial NLRP3 Inflammasome Activation upon TLR2 and TLR5 Ligation by Distinct α -Synuclein Assemblies. *J. Immunol.* 187, 2143–2154. <https://doi.org/10.4049/jimmunol.2100035>.
33. Yamamoto, M., Kiyota, T., Walsh, S.M., Liu, J., Kipnis, J., and Ikezu, T. (2008). Cytokine-Mediated Inhibition of Fibrillar Amyloid- β Peptide Degradation by Human Mononuclear Phagocytes. *J. Immunol.* 181, 3877–3886. <https://doi.org/10.4049/jimmunol.181.6.3877>.
34. Emmanouilidou, E., Melachroinou, K., Roumeliotis, T., Garbis, S.D., Ntzouni, M., Margaritis, L.H., Stefanis, L., and Vekrellis, K. (2010). Cell-Produced α -Synuclein Is Secreted in a Calcium-Dependent Manner by Exosomes and Impacts Neuronal Survival. *J. Neurosci.* 30, 6838–6851. <https://doi.org/10.1523/JNEUROSCI.5699-09.2010>.
35. Emmanouilidou, E., and Vekrellis, K. (2016). Exocytosis and Spreading of Normal and Aberrant α -Synuclein. *Brain Pathol.* 26, 398–403. <https://doi.org/10.1111/bpa.12373>.
36. Ferreira, S.A., and Romero-Ramos, M. (2018). Microglia Response During Parkinson's Disease: Alpha-Synuclein Intervention. *Front. Cell. Neurosci.* 12, 247. <https://doi.org/10.3389/fncel.2018.00247>.
37. Lee, H.-J., Patel, S., and Lee, S.-J. (2005). Intravesicular Localization and Exocytosis of α -Synuclein and its Aggregates. *J. Neurosci.* 25, 6016–6024. <https://doi.org/10.1523/JNEUROSCI.0692-05.2005>.
38. Scheiblich, H., Dansokho, C., Mercan, D., Schmidt, S.V., Bousset, L., Wischhof, L., Eikens, F., Odainic, A., Spitzer, J., Griep, A., et al. (2021). Microglia jointly degrade fibrillar alpha-synuclein cargo by distribution through tunneling nanotubes. *Cell* 184, 5089–5106.e21. <https://doi.org/10.1016/j.cell.2021.09.007>.
39. Chakraborty, R., Nonaka, T., Hasegawa, M., and Zurzolo, C. (2023). Tunneling nanotubes between neuronal and microglial cells allow bidirectional transfer of α -Synuclein and mitochondria. *Cell Death Dis.* 14, 329. <https://doi.org/10.1038/s41419-023-05835-8>.
40. Cordero Cervantes, D., and Zurzolo, C. (2021). Peering into tunneling nanotubes—The path forward. *EMBO J.* 40, e105789. <https://doi.org/10.15252/embj.2020105789>.
41. Abounit, S., Delage, E., and Zurzolo, C. (2015). Identification and characterization of tunneling nanotubes for intercellular trafficking. *Curr. Protoc. Cell Biol.* 67, 12.10.1–12.10.21.
42. Franco, S., Noureddine, A., Guo, J., Keth, J., Paffett, M.L., Brinker, C.J., and Serda, R.E. (2020). Direct Transfer of Mesoporous Silica Nanoparticles between Macrophages and Cancer Cells. *Cancers* 12, 2892. <https://doi.org/10.3390/cancers12102892>.
43. Whitelaw, B.S., Matei, E.K., and Majewska, A.K. (2020). Phosphoinositide-3-Kinase γ Is Not a Predominant Regulator of ATP-Dependent Directed Microglial Process Motility or Experience-Dependent Ocular Dominance Plasticity. *eNeuro* 7, ENEURO.0311-20.2020. <https://doi.org/10.1523/ENEURO.0311-20.2020>.
44. Cserép, C., Pósai, B., Lénárt, N., Fekete, R., László, Z.I., Lele, Z., Orsolits, B., Molnár, G., Heindl, S., Schwarcz, A.D., et al. (2020). Microglia monitor and protect neuronal function through specialized somatic purinergic junctions. *Science* 367, 528–537. <https://doi.org/10.1126/science.aax6752>.
45. Hoffmann, K., Baqi, Y., Morena, M.S., Glänzel, M., Müller, C.E., and von Kügelgen, I. (2009). Interaction of New, Very Potent Non-Nucleotide Antagonists with Arg256 of the Human Platelet P2Y₁₂ Receptor. *J. Pharmacol. Exp. Ther.* 337, 648–655. <https://doi.org/10.1124/jpet.109.156687>.
46. Cordero Cervantes, D., Khare, H., Wilson, A.M., Mendoza, N.D., Coulon-Mahdi, O., Lichtman, J.W., and Zurzolo, C. (2023). 3D reconstruction of the cerebellar germinal layer reveals tunneling connections between developing granule cells. *Sci. Adv.* 9, eadf3471. <https://doi.org/10.1126/sciadv.adf3471>.
47. The MICrONS Consortium, Bae, J.A., Baptiste, M., Bishop, C.A., Bodor, A.L., Brittain, D., Buchanan, J., Bumbarger, D.J., Castro, M.A., Celii, B., et al. (2021). Functional connectomics spanning multiple areas of mouse visual cortex. Preprint at bioRxiv. <https://doi.org/10.1101/2021.07.28.454025>.
48. Morris, M., Sanchez, P.E., Verret, L., Beagle, A.J., Guo, W., Dubal, D., Ranasinghe, K.G., Koyama, A., Ho, K., Yu, G., et al. (2015). Network dysfunction in α -synuclein transgenic mice and human Lewy body dementia. *Ann. Clin. Transl. Neurol.* 2, 1012–1028. <https://doi.org/10.1002/acn3.257>.
49. Busche, M.A., Wegmann, S., Dujardin, S., Commins, C., Schiantarelli, J., Klickstein, N., Kamath, T.V., Carlson, G.A., Nelken, I., and Hyman, B.T. (2019). Tau impairs neural circuits, dominating amyloid- β effects, in Alzheimer models in vivo. *Nat. Neurosci.* 22, 57–64. <https://doi.org/10.1038/s41593-018-0289-8>.
50. Pontes, B., Viana, N.B., Campanati, L., Farina, M., Neto, V.M., and Nussenzweig, H.M. (2008). Structure and elastic properties of tunneling nanotubes. *Eur. Biophys. J.* 37, 121–129. <https://doi.org/10.1007/s00249-007-0184-9>.
51. Önfelt, B., Nedvetzki, S., Yanagi, K., and Davis, D.M. (2004). Cutting Edge: Membrane Nanotubes Connect Immune Cells. *J. Immunol.* 173, 1511–1513. <https://doi.org/10.4049/jimmunol.173.3.1511>.
52. Saha, T., Dash, C., Jayabalan, R., Khiste, S., Kulkarni, A., Kurmi, K., Mondal, J., Majumder, P.K., Bardia, A., Jang, H.L., and Sengupta, S. (2022). Intercellular nanotubes mediate mitochondrial trafficking between cancer and immune cells. *Nat. Nanotechnol.* 17, 98–106. <https://doi.org/10.1038/s41565-021-01000-4>.
53. Forman, H.J., and Zhang, H. (2021). Targeting oxidative stress in disease: promise and limitations of antioxidant therapy. *Nat. Rev. Drug Discov.* 20, 689–709. <https://doi.org/10.1038/s41573-021-00233-1>.
54. Tolosa, E., Vila, M., Klein, C., and Rascol, O. (2020). LRRK2 in Parkinson disease: challenges of clinical trials. *Nat. Rev. Neurol.* 16, 97–107. <https://doi.org/10.1038/s41582-019-0301-2>.
55. Niu, J., Yu, M., Wang, C., and Xu, Z. (2012). Leucine-rich repeat kinase 2 disturbs mitochondrial dynamics via Dynamin-like protein: LRRK2 disturbs mitochondrial dynamics via DLP1. *J. Neurochem.* 122, 650–658. <https://doi.org/10.1111/j.1471-4159.2012.07809.x>.
56. Mortiboys, H., Johansen, K.K., Aasly, J.O., and Bandmann, O. (2010). Mitochondrial impairment in patients with Parkinson disease with the G2019S mutation in LRRK2. *Neurology* 75, 2017–2020. <https://doi.org/10.1212/WNL.0b013e3181ff9685>.
57. Thelen, M., Razquin, C., Hernández, I., Gorostidi, A., Sánchez-Valle, R., Ortega-Cubero, S., Wolfsgruber, S., Drichel, D., Fliessbach, K., Duenkel, T., et al. (2014). Investigation of the role of rare TREM2 variants in frontotemporal dementia subtypes. *Neurobiol. Aging* 35, 2657.e13–2657.e19. <https://doi.org/10.1016/j.neurobiolaging.2014.06.018>.
58. Borroni, B., Ferrari, F., Galimberti, D., Nacmias, B., Barone, C., Bagnoli, S., Fenoglio, C., Piaceri, I., Archetti, S., Bonvicini, C., et al. (2014). Heterozygous TREM2 mutations in frontotemporal dementia. *Neurobiol. Aging* 35, 934.e7–934.e10. <https://doi.org/10.1016/j.neurobiolaging.2013.09.017>.
59. Rustom, A., Saffrich, R., Markovic, I., Walther, P., and Gerdes, H.-H. (2004). Nanotubular Highways for Intercellular Organelle Transport. *Science* 303, 1007–1010. <https://doi.org/10.1126/science.1093133>.
60. Dieriks, B.V., Park, T.I.-H., Fourie, C., Faull, R.L.M., Dragunow, M., and Curtis, M.A. (2017). α -synuclein transfer through tunneling nanotubes occurs in SH-SY5Y cells and primary brain pericytes from Parkinson's disease patients. *Sci. Rep.* 7, 42984. <https://doi.org/10.1038/srep42984>.
61. Rostami, J., Holmqvist, S., Lindström, V., Sigvardson, J., Westermark, G.T., Ingelsson, M., Bergström, J., Roybon, L., and Erlandsson, A. (2017). Human Astrocytes Transfer Aggregated Alpha-Synuclein via Tunneling Nanotubes. *J. Neurosci.* 37, 11835–11853. <https://doi.org/10.1523/JNEUROSCI.0983-17.2017>.
62. Hanna, S.J., McCoy-Simandle, K., Miskolci, V., Guo, P., Cammer, M., Hodgson, L., and Cox, D. (2017). The role of Rho-GTPases and actin

polymerization during macrophage tunneling nanotube biogenesis. *Sci. Rep.* 7, 8547.

63. Lachambre, S., Chopard, C., and Beaumelle, B. (2014). Preliminary characterisation of nanotubes connecting T-cells and their use by HIV-1. *Biol. Cell* 106, 394–404.
64. Bhat, S., Ljubojevic, N., Zhu, S., Fukuda, M., Echard, A., and Zurzolo, C. (2020). Rab35 and its effectors promote formation of tunneling nanotubes in neuronal cells. *Sci. Rep.* 10, 16803.
65. Zhu, S., Bhat, S., Syan, S., Kuchitsu, Y., Fukuda, M., and Zurzolo, C. (2018). Rab11a–Rab8a cascade regulates the formation of tunneling nanotubes through vesicle recycling. *J. Cell Sci.* 131, jcs215889.
66. Schiller, C., Diakopoulos, K.N., Rohwedder, I., Kremmer, E., von Toerne, C., Ueffing, M., Weidle, U.H., Ohno, H., and Weiss, E.H. (2013). LST1 promotes the assembly of a molecular machinery responsible for tunneling nanotube formation. *J. Cell Sci.* 126, 767–777.
67. Zhang, S., Kazanietz, M.G., and Cooke, M. (2020). Rho GTPases and the emerging role of tunneling nanotubes in physiology and disease. *Am. J. Physiol. Cell Physiol.* 319, C877–C884. <https://doi.org/10.1152/ajpcell.00351.2020>.
68. Marei, H., and Malliri, A. (2017). Rac1 in human diseases: The therapeutic potential of targeting Rac1 signaling regulatory mechanisms. *Small GTPases* 8, 139–163. <https://doi.org/10.1080/21541248.2016.1211398>.
69. Cabello, J., Sámán, J., Gómez-Orte, E., Erazo, T., Coppa, A., Pujol, A., Büssing, I., Schulze, B., Lizcano, J.M., Ferrer, I., et al. (2014). PDR-1/hParkin negatively regulates the phagocytosis of apoptotic cell corpses in *Caenorhabditis elegans*. *Cell Death Dis.* 5, e1120. <https://doi.org/10.1038/cddis.2014.57>.
70. Chan, D., Citro, A., Cordy, J.M., Shen, G.C., and Wolozin, B. (2011). Rac1 Protein Rescues Neurite Retraction Caused by G2019S Leucine-rich Repeat Kinase 2 (LRRK2). *J. Biol. Chem.* 286, 16140–16149. <https://doi.org/10.1074/jbc.M111.234005>.
71. Okada, T., Hirai, C., Badawy, S.M.M., Zhang, L., Kajimoto, T., and Nakamura, S. (2016). Impairment of PDGF-induced chemotaxis by extracellular α -synuclein through selective inhibition of Rac1 activation. *Sci. Rep.* 6, 37810. <https://doi.org/10.1038/srep37810>.
72. Liu, Y.U., Ying, Y., Li, Y., Eyo, U.B., Chen, T., Zheng, J., Umpierre, A.D., Zhu, J., Bosco, D.B., Dong, H., and Wu, L.J. (2019). Neuronal network activity controls microglial process surveillance in awake mice via norepinephrine signaling. *Nat. Neurosci.* 22, 1771–1781.
73. Umpierre, A.D., Bystrom, L.L., Ying, Y., Liu, Y.U., Worrell, G., and Wu, L.-J. (2020). Microglial calcium signaling is attuned to neuronal activity in awake mice. *Elife* 9, e56502. <https://doi.org/10.7554/eLife.56502>.
74. Umpierre, A.D., and Wu, L. (2021). How microglia sense and regulate neuronal activity. *Glia* 69, 1637–1653. <https://doi.org/10.1002/glia.23961>.
75. Hristovska, I., Robert, M., Combet, K., Honnorat, J., Comte, J., and Pascual, O. (2022). Sleep decreases neuronal activity control of microglial dynamics in mice. *Nat. Commun.* 13, 6273.
76. Nebeling, F.C., Poll, S., Justus, L.C., Steffen, J., Keppler, K., Mittag, M., and Fuhrmann, M. (2023). Microglial motility is modulated by neuronal activity and correlates with dendritic spine plasticity in the hippocampus of awake mice. *Elife* 12, e83176. <https://doi.org/10.7554/eLife.83176>.
77. Badimon, A., Strasburger, H.J., Ayata, P., Chen, X., Nair, A., Ikegami, A., Hwang, P., Chan, A.T., Graves, S.M., Uweru, J.O., et al. (2020). Negative feedback control of neuronal activity by microglia. *Nature* 586, 417–423. <https://doi.org/10.1038/s41586-020-2777-8>.
78. Anwar, S., Woodling, N.S., and Niccoli, T. (2021). Mitochondria Dysfunction in Frontotemporal Dementia/Amyotrophic Lateral Sclerosis: Lessons From Drosophila Models. *Front. Neurosci.* 15, 786076. <https://doi.org/10.3389/fnins.2021.786076>.
79. Bhatti, J.S., Bhatti, G.K., and Reddy, P.H. (2017). Mitochondrial dysfunction and oxidative stress in metabolic disorders—A step towards mitochondria based therapeutic strategies. *Biochim. Biophys. Acta, Mol. Basis Dis.* 1863, 1066–1077.
80. Wang, X., and Gerdes, H.-H. (2015). Transfer of mitochondria via tunneling nanotubes rescues apoptotic PC12 cells. *Cell Death Differ.* 22, 1181–1191.
81. Pisani, F., Castagnola, V., Simone, L., Loiacono, F., Svelto, M., and Benfenati, F. (2022). Role of pericytes in blood–brain barrier preservation during ischemia through tunneling nanotubes. *Cell Death Dis.* 13, 582.
82. Ahmad, T., Mukherjee, S., Pattnaik, B., Kumar, M., Singh, S., Kumar, M., Rehman, R., Tiwari, B.K., Jha, K.A., Barhanpurkar, A.P., et al. (2014). Miro1 regulates intercellular mitochondrial transport & enhances mesenchymal stem cell rescue efficacy. *The EMBO journal* 33, 994–1010.
83. Cho, Y.M., Kim, J.H., Kim, M., Park, S.J., Koh, S.H., Ahn, H.S., Kang, G.H., Lee, J.-B., Park, K.S., and Lee, H.K. (2012). Mesenchymal stem cells transfer mitochondria to the cells with virtually no mitochondrial function but not with pathogenic mtDNA mutations. *PLoS One* 7, e32778.
84. Islam, M.N., Das, S.R., Emin, M.T., Wei, M., Sun, L., Westphalen, K., Rowlands, D.J., Quadri, S.K., Bhattacharya, S., and Bhattacharya, J. (2012). Mitochondrial transfer from bone-marrow-derived stromal cells to pulmonary alveoli protects against acute lung injury. *Nat. Med.* 18, 759–765.
85. Yang, F., Zhang, Y., Liu, S., Xiao, J., He, Y., Shao, Z., Zhang, Y., Cai, X., and Xiong, L. (2022). Tunneling nanotube-mediated mitochondrial transfer rescues nucleus pulposus cells from mitochondrial dysfunction and apoptosis. *Oxid. Med. Cell. Longev.* 2022, 3613319.
86. Jiang, D., Chen, F.-X., Zhou, H., Lu, Y.-Y., Tan, H., Yu, S.-J., Yuan, J., Liu, H., Meng, W., and Jin, Z.-B. (2020). Bioenergetic crosstalk between mesenchymal stem cells and various ocular cells through the intercellular trafficking of mitochondria. *Theranostics* 10, 7260–7272.
87. Hu, D., Niu, J., Xiong, J., Nie, S., Zeng, F., and Zhang, Z. (2018). LRRK2 G2019S Mutation Inhibits Degradation of α -Synuclein in an In Vitro Model of Parkinson's Disease. *Curr. Med. Sci.* 38, 1012–1017. <https://doi.org/10.1007/s11596-018-1977-z>.
88. Streubel-Gallasch, L., Giusti, V., Sandre, M., Tessari, I., Plotegher, N., Giusto, E., Masato, A., Iovino, L., Battisti, I., Arrigoni, G., et al. (2021). Parkinson's Disease-Associated LRRK2 Interferes with Astrocyte-Mediated Alpha-Synuclein Clearance. *Mol. Neurobiol.* 58, 3119–3140. <https://doi.org/10.1007/s12035-021-02327-8>.
89. Hsieh, C.-H., Shaltouki, A., Gonzalez, A.E., da Cruz, A.B., Burbulla, L.F., Lawrence, E.S., Schüle, B., Krainc, D., Palmer, T.D., and Wang, X. (2016). Functional impairment in miro degradation and mitophagy is a shared feature in familial and sporadic Parkinson's disease. *Cell Stem Cell* 19, 709–724.
90. Schildt, A., Walker, M.D., Dinelle, K., Miao, Q., Schulzer, M., O'Kusky, J., Farrer, M.J., Doudet, D.J., and Sossi, V. (2019). Single Inflammatory Trigger Leads to Neuroinflammation in LRRK2 Rodent Model without Degeneration of Dopaminergic Neurons. *JPD* 9, 121–139. <https://doi.org/10.3233/JPD-181446>.
91. Penney, J., Ralvenius, W.T., Loon, A., Cerit, O., Dileep, V., Milo, B., Woolf, H., and Tsai, L.-H. (2022). Distinct effects of disease-associated TREM2 R47H/+ and T66M mutations on iPSC-derived microglia. Preprint at bioRxiv. <https://doi.org/10.1101/2022.10.05.511003>.
92. Piers, T.M., Cosker, K., Mallach, A., Johnson, G.T., Guerreiro, R., Hardy, J., and Pocock, J.M. (2020). A locked immunometabolic switch underlies TREM2 R47H loss of function in human iPSC-derived microglia. *FASEB j.* 34, 2436–2450. <https://doi.org/10.1096/fj.201902447R>.
93. Alarcon-Martinez, L., Villafranca-Baughman, D., Quintero, H., Kacerovsky, J.B., Dotigny, F., Murai, K.K., Prat, A., Drapeau, P., and Di Polo, A. (2020). Interpericyte tunnelling nanotubes regulate neurovascular coupling. *Nature* 585, 91–95.
94. Alarcon-Martinez, L., Shiga, Y., Villafranca-Baughman, D., Belforte, N., Quintero, H., Dotigny, F., Cueva Vargas, J.L., and Di Polo, A. (2022). Pericyte dysfunction and loss of interpericyte tunneling nanotubes

- promote neurovascular deficits in glaucoma. *Proc. Natl. Acad. Sci. USA* 119, e2110329119. <https://doi.org/10.1073/pnas.2110329119>.
95. Walmsley, M.J., Ooi, S.K., Reynolds, L.F., Smith, S.H., Ruf, S., Mathiot, A., Vanes, L., Williams, D.A., Cancro, M.P., and Tybulewicz, V.L. (2003). Critical roles for Rac1 and Rac2 GTPases in B cell development and signaling. *Science* 302, 459–462.
96. Helwig, M., Klinkenberg, M., Rusconi, R., Musgrove, R.E., Majbour, N.K., El-Agnaf, O.M.A., Ulusoy, A., and Di Monte, D.A. (2016). Brain propagation of transduced α -synuclein involves non-fibrillar protein species and is enhanced in α -synuclein null mice. *Brain* 139, 856–870. <https://doi.org/10.1093/brain/awv376>.
97. Schindowski, K., Bretteville, A., Leroy, K., Bégard, S., Brion, J.-P., Hamdane, M., and Buée, L. (2006). Alzheimer's disease-like tau neuropathology leads to memory deficits and loss of functional synapses in a novel mutated tau transgenic mouse without any motor deficits. *Am. J. Pathol.* 169, 599–616.
98. Matikainen-Ankney, B.A., Kezunovic, N., Mesias, R.E., Tian, Y., Williams, F.M., Huntley, G.W., and Benson, D.L. (2016). Altered development of synapse structure and function in striatum caused by Parkinson's disease-linked LRRK2-G2019S mutation. *J. Neurosci.* 36, 7128–7141.
99. Kleinberger, G., Brendel, M., Mracsko, E., Wefers, B., Groeneweg, L., Xiang, X., Focke, C., Deußing, M., Suárez-Calvet, M., Mazaheri, F., et al. (2017). The FTD-like syndrome causing TREM2 T66M mutation impairs microglia function, brain perfusion, and glucose metabolism. *The EMBO journal* 36, 1837–1853.
100. Xiang, X., Piers, T.M., Wefers, B., Zhu, K., Mallach, A., Brunner, B., Kleinberger, G., Song, W., Colonna, M., Herms, J., et al. (2018). The Trem2 R47H Alzheimer's risk variant impairs splicing and reduces Trem2 mRNA and protein in mice but not in humans. *Mol. Neurodegener.* 13, 49.
101. Reinhardt, P., Schmid, B., Burbulla, L.F., Schöndorf, D.C., Wagner, L., Glatza, M., Höing, S., Hargus, G., Heck, S.A., Dhingra, A., et al. (2013). Genetic correction of a LRRK2 mutation in human iPSCs links parkinsonian neurodegeneration to ERK-dependent changes in gene expression. *Cell Stem Cell* 12, 354–367.
102. Haenseler, W., Sansom, S.N., Buchrieser, J., Newey, S.E., Moore, C.S., Nicholls, F.J., Chintawar, S., Schnell, C., Antel, J.P., Allen, N.D., et al. (2017). A highly efficient human pluripotent stem cell microglia model displays a neuronal-co-culture-specific expression profile and inflammatory response. *Stem Cell Rep.* 8, 1727–1742.
103. Wilgenburg, B. van, Browne, C., Vowles, J., and Cowley, S.A. (2013). Efficient, long term production of monocyte-derived macrophages from human pluripotent stem cells under partly-defined and fully-defined conditions. *PLoS One* 8, e71098.
104. Boussaad, I., Obermaier, C.D., Hanss, Z., Bobbili, D.R., Bolognin, S., Glaab, E., Wotyńska, K., Weisschuh, N., De Conti, L., May, C., et al. (2020). A patient-based model of RNA mis-splicing uncovers treatment targets in Parkinson's disease. *Sci. Transl. Med.* 12, eaau3960.
105. Reinhardt, P., Glatza, M., Hemmer, K., Tsytsyura, Y., Thiel, C.S., Höing, S., Moritz, S., Parga, J.A., Wagner, L., Bruder, J.M., et al. (2013). Derivation and expansion using only small molecules of human neural progenitors for neurodegenerative disease modeling. *PLoS One* 8, e59252.
106. Ghee, M., Melki, R., Michot, N., and Mallet, J. (2005). PA700, the regulatory complex of the 26S proteasome, interferes with α -synuclein assembly. *FEBS J.* 272, 4023–4033.
107. Bousset, L., Pieri, L., Ruiz-Arlandis, G., Gath, J., Jensen, P.H., Habenstein, B., Madiona, K., Olieric, V., Böckmann, A., Meier, B.H., and Melki, R. (2013). Structural and functional characterization of two alpha-synuclein strains. *Nat. Commun.* 4, 2575.
108. Grozdanov, V., Bousset, L., Hoffmeister, M., Bliederhaeuser, C., Meier, C., Madiona, K., Pieri, L., Kiechle, M., McLean, P.J., Kassubek, J., et al. (2019). Increased Immune Activation by Pathologic α -Synuclein in Parkinson's Disease. *Ann. Neurol.* 86, 593–606. <https://doi.org/10.1002/ana.25557>.
109. Peelaerts, W., Bousset, L., Van der Perren, A., Moskalyuk, A., Pulizzi, R., Giugliano, M., Van den Haute, C., Melki, R., and Baekelandt, V. (2015). α -Synuclein strains cause distinct synucleinopathies after local and systemic administration. *Nature* 522, 340–344. <https://doi.org/10.1038/nature14547>.
110. Barghorn, S., Biernat, J., and Mandelkow, E. (2004). Purification of Recombinant Tau Protein and Preparation of Alzheimer-Paired Helical Filaments In Vitro. In *Amyloid Proteins* (Humana Press), pp. 035–052. <https://doi.org/10.1385/1-59259-874-9:035>.
111. Ising, C., Venegas, C., Zhang, S., Scheiblich, H., Schmidt, S.V., Vieira-Saecker, A., Schwartz, S., Albasset, S., McManus, R.M., Tejara, D., et al. (2019). NLRP3 inflammasome activation drives tau pathology. *Nature* 575, 669–673. <https://doi.org/10.1038/s41586-019-1769-z>.
112. Sui, D., Liu, M., and Kuo, M.-H. (2015). In Vitro Aggregation Assays Using Hyperphosphorylated Tau Protein. *JoVE* 51537, e51537. <https://doi.org/10.3791/51537>.
113. Chen, T.-W., Wardill, T.J., Sun, Y., Pulver, S.R., Renninger, S.L., Baohan, A., Schreiter, E.R., Kerr, R.A., Orger, M.B., Jayaraman, V., et al. (2013). Ultrasensitive fluorescent proteins for imaging neuronal activity. *Nature* 499, 295–300. <https://doi.org/10.1038/nature12354>.
114. Connolly, N.M.C., Theurey, P., Adam-Vizi, V., Bazan, N.G., Bernardi, P., Bolaños, J.P., Culmsee, C., Dawson, V.L., Deshmukh, M., Duchen, M.R., et al. (2018). Guidelines on experimental methods to assess mitochondrial dysfunction in cellular models of neurodegenerative diseases. *Cell Death Differ.* 25, 542–572. <https://doi.org/10.1038/s41418-017-0020-4>.
115. Hefendehl, J.K., Milford, D., Eicke, D., Wegenast-Braun, B.M., Calhoun, M.E., Grathwohl, S.A., Jucker, M., and Liebig, C. (2012). Repeatable target localization for long-term in vivo imaging of mice with 2-photon microscopy. *J. Neurosci. Methods* 205, 357–363.
116. Holtmaat, A., Bonhoeffer, T., Chow, D.K., Chuckowree, J., De Paola, V., Hofer, S.B., Hübener, M., Keck, T., Knott, G., Lee, W.-C.A., et al. (2009). Long-term, high-resolution imaging in the mouse neocortex through a chronic cranial window. *Nat. Protoc.* 4, 1128–1144. <https://doi.org/10.1038/nprot.2009.89>.

STAR★METHODS

KEY RESOURCES TABLE

REAGENT or RESOURCE	SOURCE	IDENTIFIER
Antibodies		
Goat anti-Iba1	Novusbio	Cat# NB100-1028; RRID: AB_2224398
Goat anti-Mouse IgG (H + L) Alexa Fluor 488	Invitrogen	Cat# A28175; RRID: AB_2536161
Goat anti-Mouse IgG (H + L) Alexa Fluor 594	Invitrogen	Cat# A-11032; RRID: AB_2534091
Goat anti-Rabbit IgG (H + L) Alexa Fluor 488	Invitrogen	Cat# A-11008; RRID: AB_143165
Goat anti-Rabbit IgG (H + L) Alexa Fluor 594	Invitrogen	Cat# A-11012; RRID: AB_2534079
Goat anti-Rabbit IgG (H + L) Alexa Fluor 647	Invitrogen	Cat# A-21245; RRID: AB_2535813
Goat anti-Rat IgG (H + L) Alexa Fluor 488	Invitrogen	Cat# A-11006; RRID: AB_2534074
Mouse anti- α -synuclein	BioLegend	Cat# 807801; RRID: AB_2564730
Mouse anti- α -synuclein phospho (Ser129)	BioLegend	Cat# MMS-509; RRID: AB_2564891
Mouse anti-MAP2	Sigma-Aldrich	Cat# M4403; RRID: AB_477193
Mouse anti-MAPT phospho (Ser202, Thr205)	Invitrogen	Cat# MN1020; RRID: AB_223647
Mouse anti-TOMM20	Abnova	Cat# H00009804-M0; RRID: AB_519121
Mouse anti-Tuj1	Sigma-Aldrich	Cat# T8578; RRID: AB_1841228
Rabbit anti-Iba1	Wako	Cat# 019-19741; RRID: AB_839504
Rabbit anti-MAP2	Synaptic Systems	Cat# 188 003; RRID: AB_2281442
Rabbit anti-P2Y12R	Anaspec	Cat# AS-55043A; RRID: AB_2267540
Rabbit anti-TOM20	Proteintech	Cat# 11802-1-AP; RRID: AB_2207530
Rat anti-CD11b	Bio-Rad	Cat# MCA711; RRID: AB_321292
Biological samples		
<i>postmortem</i> human brain sections	Institute of Experimental Medicine, Budapest, Hungary	N/A
Chemicals, peptides, and recombinant proteins		
1,4-Dithiothreitol (DTT)	Sigma-Aldrich	Cat# 10197777001
4-(2-hydroxyethyl)-1-piperazineethanesulfonic acid (HEPES)	Thermo Fisher Scientific	Cat# J16926.22
4',6-Diamidino-2'-phenylindol-dihydrochloride (DAPI)	Thermo Fisher Scientific	Cat# 62247
6,7-Dinitroquinoxaline-2,3-dione (DNQX)	Tocris	Cat# 2312
Aqua-Poly/Mount	Polysciences	Cat# 18606
ATTO-405 NHS-ester	InvitrogenTM	Cat# A30000
ATTO-488 NHS-ester	Atto-Tec GmbH	Cat# AD 488-35
ATTO-550 NHS-ester	Atto-Tec GmbH	Cat# AD 550-35
B-27™ Plus Supplement	Gibco	Cat# A3582801
BAPTA	Invitrogen	Cat# B1205
Basal Medium Eagle (BME)	Gibco	Cat# 21010046
Bio Tracker ATP-Red Live Cell Dye	Sigma-Aldrich	Cat# SCT045
Buprenorphine hydrochloride	Indivior Eu Ltd.	PZN# 345928
Calcium chloride (CaCl ₂)	Sigma-Aldrich	Cat# 499609
Carbonyl cyanide- <i>p</i> -trifluoromethoxyphenylhydrazone (FCCP)	Sigma-Aldrich	Cat# C2920
Cefotaxime	MIP pharma	PZN# 3916283
CellTrace™ Deep Red	Thermo Fisher Scientific	Cat# C34565
CellTracer™ Violet	Thermo Fisher Scientific	Cat# C34557
Dexamethasone	Jenapharm	PZN# 8704321
DL-2-Amino-5-phosphonopentanoic acid (DL-AP-5)	Tocris	Cat# 0105

(Continued on next page)

Continued

REAGENT or RESOURCE	SOURCE	IDENTIFIER
DNase 1	Sigma-Aldrich	Cat# 11284932001
Dulbecco's Modified Eagle's Medium	Gibco	Cat# 31966047
Dulbecco's Phosphate-Buffered Saline (DPBS)	Gibco	Cat# 14190169
Fetal Bovine Serum	LIFE Technologies	Cat# 10270106
Glucose	Sigma-Aldrich	Cat# G7528
GlutaMAX™	Gibco	Cat# 35050061
Hank's Balanced Salt Solution (HBSS)	Gibco	Cat# 14170120
Heparin Sodium Salt	Sigma Aldrich	Cat# H3149
Human Serum Albumin	Sigma-Aldrich	Cat# SRP6182
Ketamine	Ratiopharm	PZN# 7538837
L-Glutamine	Gibco	Cat# 25030081
Lipopolysaccharide from Escherichia coli K12	InvivoGen	Cat# tlrl-ek
Magnesium Dichloride	Thermo Fisher Scientific	Cat# A14608.A7
Magnesium Sulfate	Thermo Fisher Scientific	Cat# 033337.36
MitoTracker™ Red FM	Invitrogen	Cat# M22425
N2-Supplement	Gibco	Cat# 17502048
Neurobasal	Gibco	Cat# 21103049
Normal Goat Serum	Abcam	Cat# ab7481
Normal Horse Serum	Abcam	Cat# ab139501
Paraformaldehyde	Sigma-Aldrich	Cat# P6148
Penicillin/Streptomycin	Gibco	Cat# 15070063
Phalloidin Alexa Fluor™ 647	Invitrogen	Cat# A22287
Phosphate-Buffered Saline	Biochrom GmbH	Cat# L 182-10
Poly-L-lysine Hybridomide	Sigma-Aldrich	Cat# P1524
Poly-D-lysine Hydrobromide	Sigma-Aldrich	Cat# P4158
Potassium Chloride	Thermo Fischer Scientific	Cat# A11662.0B
Potassium Citrate	Thermo Fischer Scientific	Cat# AC611755000
Potassium D-Gluconate	Thermo Fischer Scientific	Cat# B25135.30
Potassium Phosphate	Sigma Aldrich	Cat# P0662
Sodium Bicarbonate	Sigma-Aldrich	Cat# S5761
Sodium Chloride	Thermo Fischer Scientific	Cat# J21618.A1
Sodium Dihydrogen Phosphate Monohydrate	Thermo Fischer Scientific	Cat# AC207802500
Tat-Cre Recombinase	Merck Millipore	Cat# SCR508
Tetramethylrhodamine Methyl Ester (TMRM)	Molecular Probes	Cat# T668
Thioflavin T	Sigma-Aldrich	Cat# T3516-25G
Triton X-100	Sigma-Aldrich	Cat# X100
Trypsin-EDTA (0.5%), no phenol red	LIFE Technologies	Cat# 15400054
Wheat Germ Agglutinin Alexa Fluor 488	Thermo Fisher Scientific	Cat# W11261
Xylazine	Serumwerk Bernburg	PZN# 10124950

Critical commercial assays

CELLROX® Deep Red Flow Cytometry Assay Kit	Thermo Fisher Scientific	Cat# C10491
Pierce LAL Chromogenic Endotoxin Quantification Kit	Fisher Scientific	Cat# 88282
RNeasy Micro Kit	Qiagen	Cat# 74004
SYTOX® Blue Dead Cell stain solution	Thermo Fisher Scientific	Cat# S11348
XF Cell Mito Stress Test	Agilent	Cat# 103015-100

Plasmids

pAAV.Syn.GCaMP6f.WPRE.SV40	https://doi.org/10.1038/nature12354	Addgene, Cat# 100837
----------------------------	---	----------------------

(Continued on next page)

Continued

REAGENT or RESOURCE	SOURCE	IDENTIFIER
Deposited data		
Bulk RNA-sequencing data generated from primary neurons and primary microglia	https://www.ncbi.nlm.nih.gov/geo/	GEO: GSE209972
Experimental models		
E.coli BL21 DE3 CodonPlus cells	Aligent Technologies	Cat# 230245
Mouse: B6.Cg-Trem2 ^{em1Bwef} /J (T66M)	The Jackson Laboratory	RRID: MGI:6491229
Mouse: C57BL/6	Charles River Laboratories	RRID: IMSR_JAX:000664
Mouse: C57BL/6 Cx3cr1 ^{GFP}	The Jackson Laboratory	RRID: IMSR_JAX:005582
Mouse: C57BL/6 LRRK2 G2019S	Taconic Biosciences	RRID: IMSR_TAC:13940
Mouse: C57BL/6 Rac1 ^{flox/flox}	https://doi.org/10.1126/science.1089709	N/A
Mouse: C57BL/6 Tg(Thy1-MAPT)22Schd	https://doi.org/10.2353/ajpath.2006.060002	N/A
Mouse: C57BL/6J-Trem2 ^{em1Adiuj} /J (R47H)	The Jackson Laboratory	RRID: IMSR_JAX:027918
Software and algorithms		
Clampfit 10 software, v10	Molecular Devices	RRID: SCR_011323
FACSDIVA™ software, v9.0	Becton Dickinson	RRID: SCR_001456
Fiji ImageJ, v2.0.0-rc-69/1.52n	Wayne Rusband	RRID: SCR_002285
FlowJo, v3.05470	FlowJo, LLC	RRID: SCR_008520
ggplot2, v3.2.1	CRAN	RRID: SCR_014601
Graph Pad Prism, v8.0 and v9.0	GraphPad Software Inc.	RRID: SCR_002798
Image Studio, v5.2	LI-COR Biosciences	RRID: SCR_015795
Imaris, v9.2.1	Bitplane by Oxford Instruments plc	RRID: SCR_007370
MATLAB, 2021a	The MathWorks	RRID: SCR_001622
NIS-elements, AR 4.20.03	Nikon	RRID: SCR_014329
Partek Genomics Suite and R, v3.5.0	Parket Inc.	RRID: SCR_011860
tidyr, v1.0.2	CRAN	RRID: SCR_017102
Other		
μ-slide 8 well	Ibidi	N/A
BD FACSCANTOII	BD Biosciences	N/A
Corning® Transwell® Polycarbonate membrane-Cellculture Inserts	Sigma-Aldrich	CLS3422
CytoFLEX SRT Benchtop Cell Sorter	Beckman Coulter	N/A
EPC-10 double patch clamp amplifier	HEKA electronics	N/A
EPI-SCOPE1 Apotome	Zeiss	N/A
HiSeq2500	Illumina	N/A
Infinite M200 Pro	TECAN	N/A
Nikon Eclipse Ti fluorescence microscope	Nikon	N/A
ODYSSEY CLx Imaging System	LI-COR Biotechnology	N/A
Patch pipettes	Harvard Apparatus	N/A
PatchMaster	HEKA electronics	N/A
Pierce™ High Capacity Endotoxin Removal Spin Columns	Thermo Scientific	N/A
Schick driller C1 device	Schick GmbH	N/A
Ti:Sapphire 2-photon laser scanning microscope	Nikon	N/A
Vibratome VT1200S	Leica	N/A
XFe-24 Extracellular Flux Analyzer	Agilent	N/A
Zeiss Laser Scan Microscope 800 AiryScan	Carl Zeiss	N/A
Zeiss Laser Scan Microscope 900 AiryScan2	Carl Zeiss	N/A

RESOURCE AVAILABILITY

Lead contact

Further information and requests for resources and reagents should be directed to and will be fulfilled by the corresponding author, Michael T. Heneka (michael.heneka@uni.lu).

Materials availability

This study did not generate new unique reagents.

Data and code availability

- RNA sequencing data have been deposited at GEO and are publicly available as of the date of publication. Accession numbers are listed in the [key resources table](#). Microscopy data reported in this paper will be shared by the [lead contact](#) upon request.
- This paper does not report original code.
- Any additional information required to reanalyze the data reported in this paper is available from the [lead contact](#) upon request.

EXPERIMENTAL MODELS AND SUBJECT DETAILS

Ethical considerations

All experiments were performed following the Institutional Ethical Codex of the University Hospital Bonn – Medical Center and the University of Budapest, and the Hungarian Act of Animal Care and Experimentation guidelines (40/2013, II.14), which are in concert with the European Communities Council Directive of September 22, 2010 (2010/63/EU). The Animal Care and Experimentation Committee of the Institute of Experimental Medicine and the Animal Health and Food Control Station, Budapest, have also approved the experiments under the numbers PE/EA/1021-7/2019, and PE/EA/673-7/2019. Human brain tissue was obtained from subjects who died from causes unrelated to brain diseases (ethical approval ETT TUKEB 31443/2011/EKU [518/PI/11]). Informed consent was obtained for using brain tissue and access to medical records for research purposes. Tissue was obtained and used to comply with the Declaration of Helsinki.

Animal procedures and sample collection

All mice were on a C57BL/6N genetic background unless otherwise stated. *Rac1^{flox/flox}* mice were kindly provided by Prof. Fritz and Dr. Henninger from the Heinrich Heine University Düsseldorf.⁹⁵ Mice were housed under standard conditions at 22°C and a 12 h light-dark cycle with free access to food and water. Animal care and handling were performed according to the animal welfare guidelines laid down by the German Research Council (DFG) and approved by the local ethical committees.

Adult male wild-type mice were anesthetized by intraperitoneal injection of 0.15–0.25 mL of an anesthetic mixture (20 mg/mL ketamine, 4 mg/mL xylazine-hydrochloride). Animals were perfused transcardially with 0.9% NaCl solution for 1 min, followed by 4% freshly depolymerized paraformaldehyde (PFA) in 0.1 M phosphate buffer (PB) pH 7.4 for 40 min, and finally with 0.1 M PB for 10 min to wash the fixative out. Brains were dissected, and coronal sections were prepared on a vibratome (VT1200S, Leica, Germany) at 50 µm thickness for immunofluorescent experiments. Midbrain sections of mouse models of PD⁹⁶ at 6 months of age were used for immunostainings, whereas hippocampal sections were utilized for immunostainings of tissue deriving from 11 month old mice from the THY-Tau22 transgenic mouse model of FTD.⁹⁷

Human tissue samples

Brains of patients (two females, age 59 and 60; one male, age 73) were removed 3–5 h after death. The internal carotid and the vertebral arteries were cannulated. The brains were perfused first with physiological saline (1.5 L in 30 min) containing heparin (5 mL), followed by a fixative solution containing 4% PFA, 0.05% glutaraldehyde, and 0.2% picric acid (v/v) in 0.1 M PB, pH 7.4 (4–5 L in 1.5–2 h). The cortical samples were removed from the brains after perfusion and postfixed overnight in the same fixative solution, except for glutaraldehyde, which was excluded. Blocks were dissected, and 50 µm thick sections were prepared on a vibratome.

Primary neuronal cultures

Primary neuronal cultures were prepared from embryonic pups (E15–16) taken from pregnant female C57BL/6N mice. Brains were taken out, stripped of the meninges, and the cortices were dissected. Cortices were washed in 1x HBSS (Thermo Fisher Scientific) and dissociated into single-cell suspensions using mechanical shearing, trypsin (Life Technologies), and DNase (Roche). Depending on the experiments to be performed, 4×10^4 (calcium imaging, live cell video analysis, immunocytochemistry) or 8×10^4 (transfer experiments, electrophysiology) neurons were seeded in PDL-coated well plates or 8-well Ibidi slides in Neurobasal (NB) medium supplemented with 2% B-27 Plus and 1x L-Glutamine. Neurons were kept in culture for 7–21 days.

Primary microglia cultures

Primary microglia cultures were prepared as previously described³⁸ from WT, *Lrrk2*Gly2019Ser,⁹⁸ *Trem2*(T66M),⁹⁹ *Trem2*(R47H),¹⁰⁰ and *Rac1*^{flox/flox} pups. WT, *Lrrk2*(Gly2029Ser) and *Rac1*^{flox/flox} animals were on a C57BL/6N background, whereas *Trem2*(T66M) and *Trem2*(R47H) animals were on a C57BL/6J background. In brief, mixed glial cultures were prepared from newborn mice (P0–P3), stripped of the meninges, and dissociated using mechanical shearing and trypsin. Cells were plated on poly-L-lysine (PLL, Sigma-Aldrich) coated T75 culture flasks (Greiner bio-one) and cultivated in DMEM (Gibco) supplemented with 10% heat-inactivated fetal bovine serum (FBS; Life Technologies) and 1% penicillin/streptomycin (P/S; Gibco). After 7–10 days, mature microglia were shaken off the glial layer with a repetition of the harvesting procedure every other day up to three times. Microglia were plated according to the experiment and allowed to adhere overnight in DMEM 1%P/S and 1X N-2 supplement (Gibco). To induce *Rac1* knockout in *Rac1*^{flox/flox} microglia, cells were treated over night with 2.5 μ M tat-Cre Recombinase (Merck Millipore), followed by a washing step and a further incubation for 24 h in fresh medium without tat-Cre.

Organotypic brain slice cultures (OSCs)

WT neonatal mouse brains (P5–7) were used to prepare OSCs as described before.³⁸ In brief, brains were dissected and sectioned sagittally on a vibratome (VT1200S, Leica) to 350 μ M thick slices. Hippocampi and adjacent cortices were cultured on cell culture inserts (Merck) in BME (Gibco), HBSS (Gibco), and horse serum (Gibco) (2:1:1) supplemented with 1X GlutaMAX (Gibco) and 2% B-27 Plus (Gibco). The medium was changed every three days until DIV21.

iPSC maintenance and differentiation

A previously described isogenic pair of induced pluripotent stem cells (iPSC) consisting of a patient-derived line carrying the *Lrrk2*(Gly2019Ser) mutation and the gene-corrected counterpart were used to generate microglia.¹⁰¹ Microglia differentiation via embryonic bodies was performed following a previously established protocol.^{102,103} Small molecule neural precursor cells (smNPC) were previously derived from iPSC of three healthy individuals.¹⁰⁴ Neuronal differentiation of these smNPC lines was performed by an established protocol for deviation of midbrain dopaminergic neurons.¹⁰⁵

METHOD DETAILS

Antibodies and reagents

For tissue stainings, P2Y12R (Anaspec, AS-55043A, 1:2,000), Iba1 (Novusbio, NB100-1028, 1:500), Tom20 (Abnova, H00009804-M01, 1:500), Map2 (Synaptic, 188 003, 1:500), and Tuj1 (Sigma-Aldrich, T8578, 1:1000) were used. For cell culture stainings, anti-Iba1 (Wako, 019–19741, 1:500), anti-Map2 (Sigma-Aldrich, M4403, 1:1000), anti-CD11b (Bio-Rad, MCA711, 1:250), anti-Tom20 (Proteintech, 11802-1-AP, 1:1000), and Alexa Fluor-647 Phalloidin (Cell Signaling, 8940, 1:50) were used.

Immunohistochemical staining

Sections were washed in PB and Tris-buffered saline (TBS) followed by blocking for 1 h in 1% human serum albumin (HSA; Sigma-Aldrich) and 0.3% Triton X-100 dissolved in TBS. After this, sections were incubated in mixtures of primary antibodies overnight at room temperature. After incubation, sections were washed in TBS and incubated overnight at 4°C in the mixture of secondary antibodies, all diluted in TBS. Secondary antibody incubation was followed by washes in TBS. DAPI was used as a nuclear counterstain before sections were mounted on glass slides and coverslipped with Aqua-Poly/Mount (Polysciences). Immunofluorescence was analyzed using a Nikon Eclipse Ti-E inverted microscope (Nikon Instruments Europe B.V.) with a 60X oil immersion objective and an A1R laser confocal system.

Immunocytochemistry

Cultures were fixed in 4% PFA dissolved in PBS (Biochrom GmbH) and permeabilized using PBS containing 0.1% Triton X-100 (PTX). A blocking solution containing PTX and 5% normal goat serum (Vector Laboratories) was applied for 30 min. After this, sections were incubated in mixtures of primary antibodies overnight at 4°C. After incubation, sections were washed in PTX and incubated overnight at 4°C in the mixture of secondary antibodies, all diluted in PTX. DAPI was used for nuclear and Wheat Germ Agglutinin (WGA, Thermo Fisher Scientific) coupled to Alexa Fluor 488 for membrane counterstaining at 0.1 mg/mL and 0.01 mg/mL for 20 min in PBS. Images were taken using a Nikon Eclipse Ti-E inverted microscope or a Zeiss LSM 800 or 900 confocal microscope.

Electron microscopy

On neuronal DIV7, neurons and microglia were co-cultured for 6 h before fixation in Karnovsky's fixative comprising 2.5% PFA and 2.5% glutaraldehyde in 0.1 M sodium cacodylate buffer (pH 7.4) for 1 h at room temperature and another 24 h at 4°C. After fixation, co-cultures were washed three times in 0.1 M cacodylate buffer and dehydrated with ascending concentrations of alcohol and acetone before removing liquids with hexamethyl[1]disilazane (HMDS). Dried samples were attached to metal stubs covered with carbon foil and sputtered with 4 nm of platinum. Co-cultures were visualized using a JSM-7500F Field Emission Scanning Electron Microscope (JEOL).

Recombinant α -syn preparation

Human wild-type α -syn was expressed in and purified from E. coli BL21 DE3 CodonPlus cells (Agilent Technologies),¹⁰⁶ and assembled into the fibrillar polymorph “fibrils” described previously.¹⁰⁷ All α -syn preparations were quantified for endotoxin levels as previously described^{108,109} to prove that endotoxin levels were below 0.02 endotoxin units/ μ g (EU/ μ g) using the Pierce LAL Chromogenic Endotoxin Quantification Kit. α -syn fibrils were labeled with ATTO-405 NHS-ester, ATTO-488 NHS-ester, or ATTO-550 NHS-ester (Atto-Tec GmbH) fluorophore as previously described.³⁸ The fibrillar nature of α -syn was assessed by Transmission Electron Microscopy (TEM). α -syn fibrils were fragmented by sonication as described previously.³⁸

Recombinant tau preparation

Human P301S (1N4R) tau-protein was expressed in and purified from E. coli BL21 DE3 CodonPlus cells (Agilent Technologies) and assembled into the fibrillar polymorph “fibrils” as described previously.^{110,111} Appropriate endotoxin levels were ensured by Pierce High Capacity Endotoxin Removal Spin Columns (Thermo Scientific). Fibrillation was induced by Heparin (5 mM, Sigma-Aldrich) and DTT (10 μ M, Sigma-Aldrich) for 72 h and verified by Thioflavin T (20 μ M, Sigma-Aldrich) assay as described before.¹¹² Tau-fibrils were labeled with ATTO488 NHS-ester (Atto-Tec GmbH) and fragmented by sonication.

α -syn, tau, and mitochondria transfer experiments

Neurons (DIV14, 8×10^5 cells/well) were loaded for 16 h with 0.2 μ M Atto488-labelled α -syn fibrils or 0.2 μ M Atto-488-labelled tau fibrils. Microglia were labeled with CellTracer Violet (Thermo Fisher Scientific, 1:2,000). For phagocytosis experiments, neurons were labeled with CellTracer Deep Red (Thermo Fisher Scientific, 1:2,000). For mitochondria transfer experiments, neurons were labeled with CellTracer Violet, while microglia were labeled elsewhere with MitoTracker Red FM (Thermo Fisher Scientific, 1:2,000, 30 min). Labeling reaction was stopped with DMEM containing 10% FCS, discarded, and replaced by a serum-free medium. Microglia were seeded on top of neurons at a density of 1.25×10^5 cells per well for 1–6 h. For degradation experiments, cells were left in co-culture for 48 h. Co-cultures were collected, resuspended in 100 μ L ice-cold PBS +2% FCS, and measured by flow cytometry using the FACS CANTO II and the FACS DIVA software (Becton Dickinson). Cell-to-cell transfer of α -syn, tau, and/or mitochondria was then analyzed and quantified using FlowJo, LLC (v3.05470).

Electrophysiology

On DIV14–17, neurons were treated for 16 h with 0.1 μ M α -syn fibrils or left untreated (control). Following incubation, cultures were washed with pre-warmed NB medium to remove excess protein. Microglia (8×10^4) were added on top of neurons for 6 h. For electrophysiological recordings, coverslips were transferred to artificial cerebrospinal fluid (aCSF) consisting of 120 mM NaCl, 4.3 mM KCl, 1.25 mM NaH_2PO_4 , 0.5 mM MgSO_4 , 1.4 mM CaCl_2 , and 20 mM glucose. The pH was adjusted to 7.3 by gassing with carbogen (95% O_2 , 5% CO_2). The liquid junction potential was corrected for (10 mV). Recordings were performed at 32°C. Patch pipettes (4–5 M Ω resistance) made of borosilicate glass (GC150T-10, Harvard Apparatus) were pulled on a vertical puller (PA-10, E.S.F. Electronic). The intracellular solution contained 10 mM NaCl, 88 mM potassium gluconate, 20 mM potassium citrate, 10 mM HEPES, 3 mM BAPTA, 0.5 mM CaCl_2 , 1 mM MgCl_2 , 3 mM MgATP, 0.5 mM NaGTP, and 15 mM phosphocreatin, pH adjusted to 7.25. Whole-cell voltage-clamp recordings were performed at a holding potential of –60 mV using an EPC-10 double patch clamp amplifier (HEKA electronics). Current-clamp recordings were performed at resting membrane potential. In a subset of experiments, the glutamate receptor antagonists DNQX (6,7-Dinitroquinoxaline-2,3-dione, 10 μ M, Tocris) and DL-AP-5 (DL-2-Amino-5-phosphonopentanoic acid, 50 μ M, Tocris) were used to inhibit excitatory postsynaptic currents. Data were recorded using PatchMaster (HEKA electronics), digitized at 10 kHz, and analyzed offline using Clampfit 10 software (Molecular Devices). Datasets were low-pass filtered (8-pole Bessel filter; –3 dB cut-off at 40 Hz), and burst-like events were detected using the threshold function.

Calcium imaging

On DIV14, neurons were transduced by an AAV1 carrying a GFP-coupled calcium sensor expressed under the Synapsin promoter (pAAV.Syn.GCaMP6f.WPRE.SV40, kindly provided by Douglas Kim & GENIE Project, Addgene viral prep #100837-AAV1).¹¹³ On DIV16–18, neurons were treated for 16 h with 0.2 μ M α -syn or tau fibrils. Following incubation, cultures were washed to remove excess protein. Microglia (5×10^4) were seeded on top of neurons for 6–24 h. Calcium signals were captured using a Nikon Eclipse Ti-E microscope at >37 fps for 2 min. In each well, two randomly assigned positions were recorded. Datasets were analyzed by FIJI (ImageJ), and intensity changes of active cells over time were identified and extracted. Intensity changes ($\Delta F/F$) were further processed and analyzed for peak frequency, peak amplitude, and peak half-width using MATLAB (The MathWorks). Five randomly assigned neurons per recording were selected for further statistical analysis.

Live cell imaging

On DIV6, neurons were incubated eighter with 0.2 μ M Atto488-labelled α -syn fibrils or 0.2 μ M Atto-488-labelled tau fibrils for 16 h. Following incubation, cultures were washed to remove excess protein. Microglia (5×10^4) were seeded on top of neurons immediately before starting imaging. Imaging was performed using the Nikon Eclipse Ti-E, and brightfield and fluorescence images were recorded every minute at 40X magnification. Videos were analyzed using FIJI (ImageJ) to quantify particle area, total travel distance, mean velocity, and total time to travel from neuron to microglia.

ROS release and SYTOX staining

The generation of reactive oxygen species (ROS) was determined using the CellROX Deep Red Flow Cytometry Assay Kit (LIFE Technologies). In brief, neurons were treated for 16 h with 0.2 μ M α -syn fibrils or tau fibrils and incubated as described above. Cells were collected and cultured in DMEM containing 500 nM of the CellROX Deep Red reagent for 45 min at 37°C. During the final 15 min of staining 1 μ M SYTOX Blue Dead Cell stain solution was added to the cells. Cells were then assessed by flow cytometry.

Oxygen consumption rate assessment

Cellular oxygen consumption rate (OCR) was measured using an XFe-24 Extracellular Flux Analyzer together with the XF Cell Mito Stress Test (all Seahorse Agilent). On DIV14, neurons (1.2×10^5 cells/well) were treated for 16 h with 0.1–0.2 μ M α -syn fibrils or tau fibrils. Prior to the experiment, cells were equilibrated for 60 min in a CO₂-free incubator at 37°C. Bioenergetic recordings were then performed via the sequential administration of oligomycin (0.5 mM), FCCP (2 mM), and rotenone/antimycin A (0.5 mM) according to the manufacturer's protocol. Cells were lysed in RIPA buffer (Sigma Aldrich), and protein concentrations were determined via Bradford assay. OCR values were then normalized to the respective protein contents.

Imaging and mitochondrial analysis

Fluorescently stained cells were imaged using a confocal microscope with Airyscan (Zeiss LSM800) and a 63x oil immersion objective. Z-stacks (0.5 μ m steps) were taken from at least 20 cells per condition. Maximum intensity projections were then used for the semi-automatic assessment of mitochondrial morphology. Following background subtraction, a mitochondrial mask was obtained based on Tom20-positive labeled structures using the Gaussian blur and Auto Threshold (method Default) function. Mitochondrial length and shape were then analyzed via the 'Skeletonize' and 'Particle analyzer' plugins. Elongation score was calculated as $1/\text{circularity}$ ($\text{circularity} = 4 \cdot \pi \cdot (\text{area}/\text{perimeter}^2)$).

TMRM measurements

Mitochondrial membrane potential measurements were performed as described previously with slight modifications.¹¹⁴ Briefly, cortical neurons were seeded onto glass-bottom Petri dishes (1×10^5). On DIV7, neurons were treated for 16 h with 0.2 μ M α -syn fibrils, followed by three washing steps with pre-warmed NB medium. Microglia (8×10^4) were added on top of neurons for 6 h. Cells were washed with pre-warmed experimental buffer (120 mM NaCl, 3.5 mM KCl, 0.4 mM KH₂PO₄, 5 mM NaHCO₃, 20 mM HEPES, 1.2 mM Na₂SO₄, 1.2 mM CaCl₂, 2 mM MgCl₂, and 5 mM glucose) and incubated in an experimental buffer supplemented with 10 nM tetramethylrhodamine methyl ester (TMRM; Molecular Probes) for 45–60 min at 37°C in a CO₂-free incubator. Cultures were imaged using an epifluorescence microscope (EPI-SCOPE1 Apotome, Zeiss) and a 63x oil immersion objective at 1 min intervals. Following 10 min of baseline measurements, 10 μ M of the mitochondrial uncoupler FCCP was added to collapse mitochondrial membrane potential. Image processing and analysis were done using ImageJ. First, regions of interest (ROIs, i.e., somata from individual cells) were identified, and the average signal intensity within the ROI was measured. Normalized signal intensities (i.e., average fluorescence intensities after subtraction of TMRM signal following the addition of FCCP) were then plotted over time. At least 20 cells from three different neuronal preparations were analyzed.

ATP measurements

ATP levels were measured using the BioTracker ATP-Red live cell dye (Merck Millipore) according to the manufacturers protocol. Briefly, cortical neurons were seeded onto glass-bottom 8-well chamber slides (ibidi) (4×10^4). On DIV14, neurons were treated for 16 h with 0.2 μ M fluorescently labeled α -syn fibrils, followed by three washing steps with pre-warmed NB medium. CellTracer Violet-labeled microglia (4×10^4) were then added on top of the neurons for 6 h. After co-culture, cells were incubated with BioTracker ATP-Red live cell dye for 15 min, washed with warm PBS, and imaged using a confocal microscope.

RNA sequencing analysis

We used the above-described co-culture strategy and performed RNA sequencing analysis as described previously³⁸ to determine transcriptomic changes. In brief, upon co-culture, cells were sorted back into neuronal and microglial populations by flow cytometrical cell sorting (CytoFLEX SRT Benchtop Cell Sorter, Beckman Coulter), and RNA was collected using 700 μ L Trizol. Isolation of bulk RNA was performed with the RNeasy Micro Kit (Qiagen). Library production for 3'-mRNA sequencing was performed with up to 125 ng purified RNA according to the manufacturer's protocol and sequenced on a HiSeq2500 (Illumina) with a sequencing depth of 15 Mio reads per sample (NGS Core Facility, University Hospital, Bonn, Germany). Transcripts were quantified with the Partek E/M algorithm and further processed for normalization in R with the DEseq2 algorithm. Batch effects derived by independent experiments were removed in the Partek Genomics Suite (v7.18.0402). The dataset was further optimized by flooring transcripts with minimal gene counts of at least ≤ 1 and excluding transcripts with a mean expression of ≤ 10 in every test condition. Data visualization and biological interpretation were performed with the Partek Genomics Suite and R (v3.5.0), packages ggplot2 (v3.2.1) for graphical visualization of expression data, and tidy (v1.0.2) for data wrangling.

Cranial window placement and intracranial engraftment of primary cortical neurons

Cranial window installation and *in vivo* two-photon image acquisition were carried out as previously described elsewhere.^{115,116} Briefly, 7-month-old *Cx3cr1^{GFP+/-}* mice received an intraperitoneal injection (i.p.) of 1.5 mg/kg ketamine and 0.1 mg/kg xylazine,

followed by subcutaneous injections (s.c.) of 0.1 mg/kg buprenorphine, 6 mg/kg dexamethasone, and 7 mg/kg cefotaxime. Betanthen eye ointment was applied to the eyes to avoid drying. Surgical instruments were sterilized in a bead heater (GerminatorTM 500; CellPoint Scientific Inc. Gaithersburg, MD, USA) and hairs on top of the head were removed. The mouse was put into a stereotactic frame and the disinfected skin was removed using sharp scissors. The periosteum was removed by gently scraping with a scalpel to increase the gluing capacity between the ring and the skull. A small hole was drilled into the skull using a Schick Driller C1 device (Schick GmbH, Schemmerhofen, Germany). Thereafter the mouse received a stereotaxic injection of 1 μ L α -syn-loaden, CellTracer Violet labeled primary cortical neurons (1×10^6 cells/ μ L) with a speed of 0.1 μ L/min for each hole in the cortex. After the injection, the needle was kept in place for an additional 10 min before it was slowly withdrawn to avoid reflux up the needle tract. Right after, a 4 mm diameter craniotomy was performed over the right hemisphere and the craniotomy was rinsed with physiological saline solution. Subsequently, using UV-activated dental cement (Venus flow syringe assortment, MW dental) a 5-mm coverslip was placed on the top of the cranial window. A custom-made titanium ring was glued on the skull with the help of Pattex super glue gel. After the operation, the mouse was put under infrared light for recovery. The body temperature was controlled throughout the procedure and maintained at 37°C. After 24 h, two-photon imaging was performed.

***In vivo* two-photon imaging**

A Ti:Sapphire two-photon laser scanning microscope was used with a Nikon water-immersion objective (25 \times , 1.10 NA) and Nikon NIS Elements AR 4.20.03 (Build 995; Düsseldorf, Germany). Imaging was performed under isoflurane anesthesia (1.5%, flow \sim 800 mL/min). The mouse was put onto a heating blanket and rectal temperature was kept constant at 37°C. All images were taken using 920 nm wavelength for EGFP, RFP, and BFP. An overview stack was taken for orientation before areas of interest were randomly chosen. For time-lapse recordings, images were taken every 30 s.

QUANTIFICATION AND STATISTICAL ANALYSIS

Each n represents an independent biological sample. Data were evaluated using Graph Pad Prism and presented as mean \pm SEM of at least three independent experiments. Data were analyzed for Gaussian distribution. When data passed the normality test, statistical comparisons of vehicle controls versus treatment were performed with one-way ANOVA or two-way ANOVA followed by a Tukey's test. Otherwise, data were analyzed with the Kruskal-Wallis test and Dunn's post hoc test for non-parametric data. Levels of significance are indicated as * p < 0.05; ** p < 0.01; *** p < 0.001; **** p < 0.0001.